Pure Appl. Chem., Vol. 78, No. 6, pp. 1265–1298, 2006.
doi:10.1351/pac200678061265

Plasma-assisted combustion*

A. Yu. Starikovskii‡, N. B. Anikin, I. N. Kosarev, E. I. Mintoussov, S. M. Starikovskaia, and V. P. Zhukov

Physics of Nonequilibrium Systems Laboratory, Moscow Institute of Physics and Technology, Dolgoprudny, 141700, Russia

Abstract: This paper presents an overview of experimental and numerical investigations of the nonequilibrium cold plasma generated under high overvoltage and further usage of this plasma for plasma-assisted combustion.

Here, two different types of the discharge are considered: a streamer under high pressure and the so-called fast ionization wave (FIW) at low pressure.

The comprehensive experimental investigation of the processes of alkane slow oxidation in mixtures with oxygen and air under nanosecond uniform discharge has been performed. The kinetics of alkane oxidation has been measured from methane to decane in stoichiometric and lean mixtures with oxygen and air at room temperature under the action of high-voltage nanosecond uniform discharge.

The efficiency of nanosecond discharges as active particles generator for plasma-assisted combustion and ignition has been investigated. The study of nanosecond barrier discharge influence on a flame propagation and flame blow-off velocity has been carried out. With energy input negligible in comparison with the burner's chemical power, a double flame blow-off velocity increase has been obtained. A signicant shift of the ignition delay time in comparison with the autoignition has been registered for all mixtures.

Detonation initiating by high-voltage gas discharge has been demonstrated. The energy deposition in the discharge ranged from 70 mJ to 12 J. The ignition delay time, the velocity of the flame front propagation, and the electrical characteristics of the discharge have been measured during the experiments. Under the conditions of the experiment, three modes of the flame front propagation have been observed, i.e., deflagration, transient detonation, and Chapman–Jouguet detonation. The efficiency of the pulsed nanosecond discharge to deflagration-to-detonation transition (DDT) control has been shown to be very high.

Keywords: plasma; discharge; ignition; combustion; flame.

INTRODUCTION

Low-temperature plasmas came into application to technological processes in the 1970s. In the recent 10–15 years, the development of plasma chemical technologies, new experimental methods of investigation, and rapid advances in computer techniques have resulted in a revision of the approach in description of gas discharges. The development of plasma chemical technologies is determined in many respects by a degree of insight into the processes taking place in the plasma. The processes of active

*Paper presented at the 17th International Symposium on Plasma Chemistry (ISPC 17), Toronto, Ontario, Canada, 7–12 August 2005. Other presentations are published in this issue, pp. 1093–1298.

‡Corresponding author: E-mail: astar@neq.mipt.ru

particle production, which are closely related to the electric field distribution and electron kinetics, play a crucial role from the viewpoint of their applications. It is a precisely detailed investigation of gas discharge elementary processes that can improve our understanding of fundamental problems of low-temperature plasma physics and also lead to some optimal solutions of technological problems.

The problem of the uniform ignition and efficient combustion of a gas mixture is of fundamental importance from both scientific and technological standpoints. The oxidization of a fuel proceeds via a chain mechanism, which is very fast. The delay time of ignition is limited by the rate at which the active centers are produced, usually by thermal dissociation. For this reason, the total rate of reaction is, in fact, higher when a chain is artificially initiated. The easiest way to produce free radicals is to decompose the weakest bond of a molecule [1]. Two mechanisms by which a discharge can affect a gas should be taken into account when using a discharge to initiate combustion. For discharges resulting in the formation of an equilibrium (or nearly equilibrium) plasma (e.g., sparks and arcs), the main factor that reduces the delay time of ignition is local heating of gas and, accordingly, the increase in the rate of thermal dissociation [2–4]. In case of nonequilibrium plasma, the main mechanism initiating chain reactions is a dissociation and excitation of molecules by an electron impact. The question of the efficiency of using nonequilibrium plasmas still remains open despite the fact that theoretically even a relatively small amount of atoms and radicals ($\sim 10^{-5}$–10^{-3} of the total number of the gas particles) can shift the equilibrium in the system and initiate a chain reaction.

In the present paper, we analyze two radical-influenced chemically reacting systems, i.e., plasma-assisted combustion of premixed fuel–air mixtures under atmospheric conditions and the plasma-assisted ignition of homological series of hydrocarbons in the preliminary heated mixtures.

One of the possible applications of plasma-supported ignition is the length of deflagration-to-detonation transition (DDT) reduction with simultaneous minimization of the energy of initiation. Within the limits of the present work, we have studied the DDT initiated by a nonequilibrium plasma of a nanosecond gas discharge.

OXIDATION OF C_1–C_{10} HYDROCARBONS IN STOICHIOMETRIC AND LEAN MIXTURES WITH AIR AND OXYGEN UNDER THE ACTION OF NANOSECOND DISCHARGE

The experimental set-up scheme is presented in Figure 1. The electric pulses yielded to the discharge cell (DC) through 50-Ohm RF cable with 20-m length. The DC consisted of a thin-wall quartz discharge tube with 4.7-cm inner and 5-cm outer diameters, a metallic screen, and high- and low-voltage electrodes. The screen was made of eight brass rods with 12-mm diameters uniformly installed at 7-cm distance from the cell axis. The high-voltage electrode had a conical form with 60° opening angle. The low-voltage electrode was a ring directly connected to the screen. The distance between the edges of the electrodes was 20 cm.

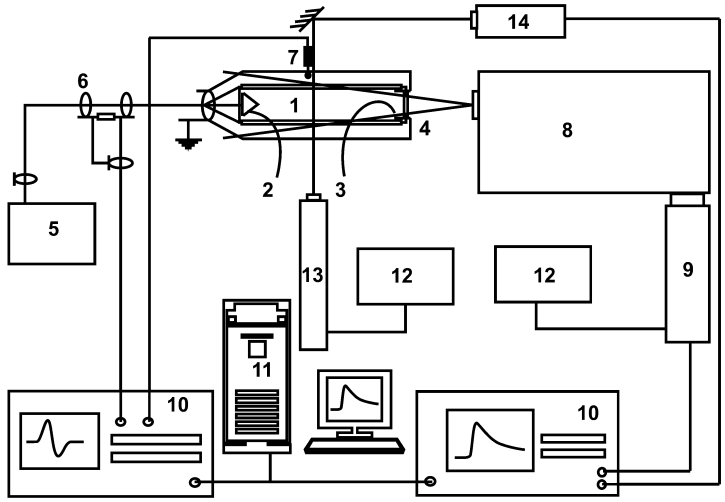

Fig. 1 Experimental set-up: 1: DC; 2,3: electrodes; 4: optical window (CaF_2); 5: HVG; 6: back-current shunt; 7: capacitive gauge; 8: monochromator; 9: photomultiplier FEU-100; 10: oscilloscopes S9-8 and TDS-380; 11: computer; 12: power supplies; 13: He–Ne laser (λ = 3.3922 μm); 14: photodetector Pb–Se.

Electrical characteristics of the discharge were measured by a capacitive gauge moving along the DC axis and a back-current shunt mounted into the break of the supplying cable screen. The back-current shunt was installed at a distance from the DC; in this case, the incident and reflected current pulses are separated in time.

In all mixtures, the emission intensity of the discharge was measured both in time-resolved (the band was 150 MHz) and in integral regimes. Emission intensities were measured through the optical CaF_2 window mounted in the low-voltage ring electrode using a monochromator MDR-23 and a photomultiplier FEU-100 (the signal rise-time was not longer than 3 ns, and the spectral sensitivity bandwidth was 200–800 nm).

Except for the potential distribution along the discharge tube, all time-resolved measurements were fulfilled using averaging over 128 pulses (in our case, the time of averaging was 3.2 s). The measurements of temporal-space dynamics of the potential distribution were performed only in the reaction products.

In the mixtures with methane, the absorption of He–Ne laser emission on 3.33922 μm was measured in addition to the general set of parameters.

The time-resolved signals were registered by oscilloscope Tektronix TDS 380 (band pass was 400 MHz). The integral measurements were performed by digital oscilloscope S9-8.

The mixtures of heavy hydrocarbons were prepared under condition that the partial pressure of the alkane was lower than the saturated vapor pressure at room temperature. A portion of the alkane was injected into the 10-liter vacuum chamber. The mass of the portion was 20 % smaller than the mass of the saturated vapor pressure of this alkane in this volume at room temperature. The control of the gas pressure in the volume allowed us to measure the alkane concentration in the volume. Later, we filled the volume with oxygen up to the required pressure.

Experimental methods

Finding electric current, electric field, and energy input

The distribution of the potential along the DC $V_i(t)$ was measured by a capacitive gauge mounted sequentially in sections x_i = 0.0; 3.6; 7.2; 10.8; 14.4; 18.0 cm. Section x_0 = 0.0 corresponded to the edge of the conical electrode.

Taking into account the inductance and the capacity of the DC, the current through the high-voltage electrode and the potential distribution along the DC were measured experimentally. These values were transformed into the current ($J(x,t)$) and the electric field distribution ($E(x,t)$) along the DC. The obtained values $E(x,t)$ and $J(x,t)$ were used to calculate the dynamics of the contributed power per unit volume $P(x,t) = E(x,t)J(x,t)/S$ (S is a square of the discharge tube cross-section).

The method used for the reconstruction provided a possibility to obtain the distribution of the electric field within the time range that was important for gas excitation. The list of alkane percentages in all investigated mixtures is presented in Table 1.

Emission spectroscopy: Experimental investigation of optical characteristics of the discharge

The control of emission intensity has been carried out for a set of spectral transitions. Table 2 presents the transitions that were controlled in all mixtures.

In addition, in air-contained mixtures we have measured the emission of $NO(A^2\Sigma \rightarrow X^2\Pi, \delta v = 3)$,

$N_2(C^3\Pi, v' = 1 \rightarrow B^3\Pi, v'' = 7)$,

$N_2(B^3\Pi, v' = 6 \rightarrow A^3\Sigma, v'' = 3)$, and

$N_2^+(B^2\Sigma, v' = 0 \rightarrow X^2\Sigma, v'' = 2)$ systems.

It is necessary to note that the intensities of the transitions of these molecules were so large that the emission of the overlapped bands was negligible.

In the case of an essential overlap of the emitted bands in order to identify the band, the emission intensities were measured in the time-resolved regime, for instance, at the time when the discharge was switched on and when the oxidation process was over (when the signal from the photomultiplier reached the steady-state value). Moreover, the measurements of the emission intensities in the time-resolved regime were used to obtain the quenching rate constants in the initial and final mixtures (reagents and products). Taking into account the constant rates of the quenching, the excitation rates of the higher states have been obtained.

Absorption spectroscopy: Methane concentration measurements

The methane concentration was measured by absorption of the emission of the He–Ne laser LGN-118 (λ = 3.3922 μm). The laser emission, whose wavelength is practically the same as the wavelength of the vibrational transition of the asymmetric mode of the CH_3-group vibration, propagated through the DC perpendicularly to its axis and came to the PbSe photoresistor (the spectral sensitivity band is 2–4 μm). Filling the DC by the mixture, we simultaneously registered pressure of the mixture and IR laser radiation absorption. Knowing the composition of the mixture and having obtained the dependence between the absorption and the mixture pressure $I(p)$, it was possible to produce the calibration curve $I([CH_4])$ for every experiment. The list of alkane percentages in all investigated mixtures is presented in Table 1.

Table 1 Investigated mixtures.

Alkane	CH_4	C_2H_6	C_3H_8	C_4H_{10}	C_5H_{12}	C_6H_{14}
With O_2	33.3	22.2	16.6	13.3	11.1	9.5
With air	11.11	–	–	–	3.03	2.56

Table 2 Transitions, controlled in all mixtures.

λ nm	$\delta\lambda$ nm	Band
518.6	2.8	CO Angstrom, $CO(B^1\Sigma, v' = 0 \rightarrow A^1\Pi, v'' = 2)$
430	3	$CH(A^2\Delta, v' = 0 \rightarrow X^2\Pi, v'' = 0)$
307.8	3.4	$OH(A^2\Sigma, v' = 0 \rightarrow X^2\Pi, v'' = 0)$
290	2.8	$CO_2^+(B^2\Sigma \rightarrow X^2\Pi, \delta v = 0)$

Plasma chemistry at low-temperature conditions

Electrodynamic description of the discharge

The measurements of the distributions of the potential, the current, the reduced electric fields, and the power per unit volume along the discharge gap obtained from the capacitive gauge and the shunt in the methane–air stoichiometric mixture are presented in Fig. 2. As a whole, the electrodynamic situation of the discharge in a relatively short discharge gap is comprehensive and essentially differs from the situation in the long gap [5]. The typical values of the fast ionization wave (FIW) velocity amounted to 23 cm/ns, and the time of the wave propagation along the DC was 7–15 ns, which was shorter than the pulse duration. Because of this feature, the short-circuit regime, which was not observed in the work [5], was registered in our experiments. In this regime, the electric field density and the current do not vary along the DC and change in time relatively slow. For example, under the pressure $p = 6.05$ Torr, this stage began at $t = 10$ ns [6].

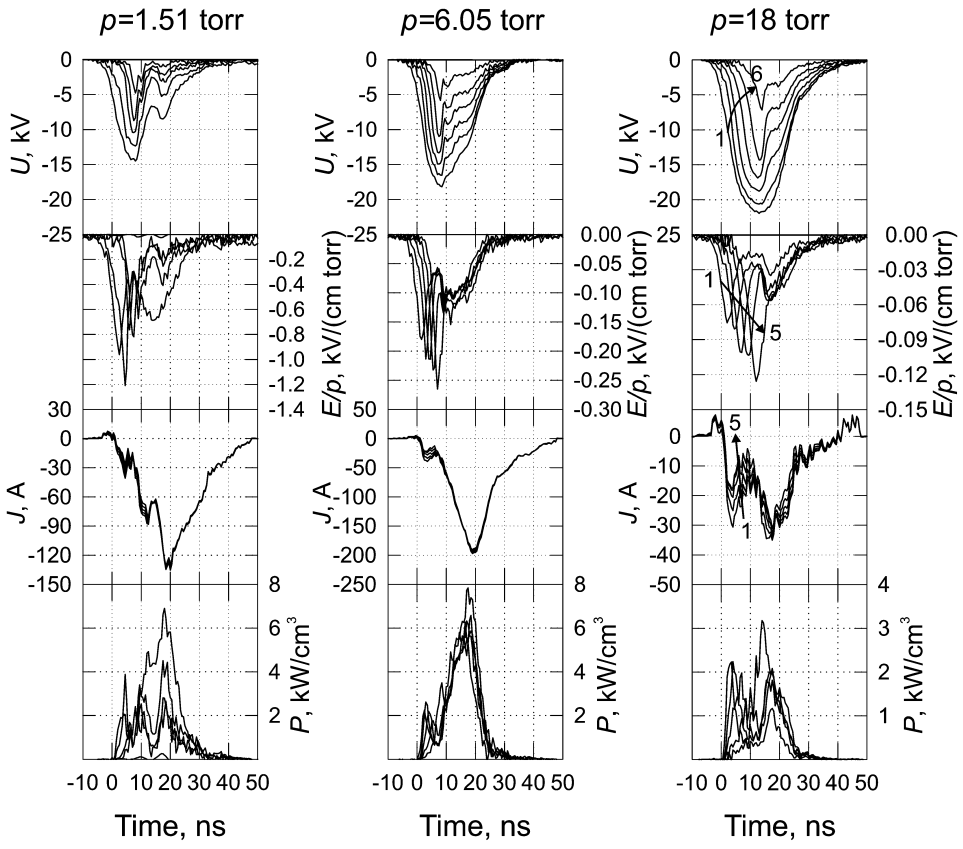

Fig. 2 Electrodynamics characteristics in the first high-voltage pulse for three different pressures—1.51, 6.05, and 18 Torr. Potential distributions $U(t)$ are presented in sections x = 0.0, 3.6, 7.2, 10.8, 14.4, 18.0 cm. Distributions of reduced electric fields $E(t)/p$, currents $J(t)$, volumetric power densities $W(t)$ averaged over the intervals are represented for the intervals 0.0–3.6, 3.6–7.2, 7.2–10.8, 10.8–14.4, and 14.4–18.0 cm. Curves are enumerated from 1 to 6 for the potential and from 7 to 12 for other values, respectively. Arrows in figures show directions of curves shifts with the consequent change from the 1st to the 6th section for voltage and from the 1st to 5th interval for other values. The mixture is the products of oxidation of CH_4 in methane–air stoichiometric mixture.

Under low pressures (p < 4 Torr), both the development of the ionization wave and the stage of the short circuit take place under a high cathode potential drop. It is important to note that the electric field in the cathode layer at p < 4 Torr is essentially higher (by the orders of magnitude) than it is shown in Fig. 3 owing to the essential value (about screen diameter) of the half-width of the sensitivity function of the capacitive gauge [5]. The thickness of the cathode layer can be estimated using the theory of glow discharge. During our experiment, the cathode layer corresponded to the case of the anomalous glow discharge, since the typical current density amounted to some A/cm^2, that is by 3–4 of the order of magnitude more than the normal current density. From this, it directly follows that the parameter (pd) was approximately equal to the value $(pd)_{\text{norm}}/e$ [Torr·cm] [7], where d is the cathode layer width, $(pd)_{\text{norm}}$ is the normal reduced cathode layer width. For the aluminum cathode in air $(pd)_{\text{norm}} \approx 0.25$ [Torr·cm] [7] that yields $pd \approx 0.09$ [Torr·cm], for the pressure p = 0.76 Torr d is 1.2 mm, and for the pressure p = 9.83 Torr d is 100 μm.

As shown above, some part of the pulse reflected from the DC and returned to the generator, then it reflected from the generator and came to the DC again. The discharge initiated by these secondary pulses was formed immediately at the stage of the short circuit. No cathode drop in these pulses was

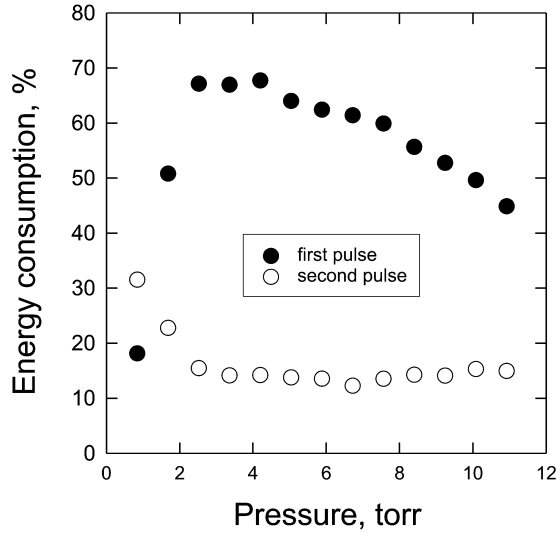

Fig. 3 The energy input in the discharge for the first and the second pulses in the processed methane–air mixture depending on the initial pressure of the mixture.

observed for the pressure higher than 0.76 Torr, and thus the energy contribution in these pulses was uniform.

The dependence between the energy contribution and the pressure is shown in Fig. 3. It is clearly seen that for the pressure of 0.76 Torr, the energy contribution in the second pulse is higher than that in the first pulse. With the growth of pressure, the energy contribution increases and reaches the maximum value approximately at pressure 3.5 Torr, while the energy contribution in the second pulse decreases and beginning with pressure 3.5 Torr, it becomes constant. The energy contribution in the third and other pulses is lower than 2 %. It is important to note that the high value of energy contribution in the second pulse partially compensates nonuniformity of the contribution at low pressures. Thus, the main part of energy within the pressure range (0.76–10.6 Torr), where the investigations were carried out, is contributed into the gas on the stage of the short circuit in the first or the second pulse.

Figure 4 presents the energy contribution represented by all investigated mixtures at the beginning of the discharge and after the oxidation process. The total energy of the pulse reaches 60 mJ. It is seen from Fig. 4 that at the beginning of the oxidation process the energy contribution to any mixture with oxygen for pressures higher than 3 Torr is systematically higher than that for a mixture with air. With the growth of the pressure, the difference increases and reaches 12 % for p = 10.6 Torr. In processed mixtures, the variations of the energy contribution from mixture to mixture are negligible and even the presence of nitrogen does not effect essentially the energy contribution. The energy contribution is higher only in the methane–oxygen processed mixture than that one in other mixtures.

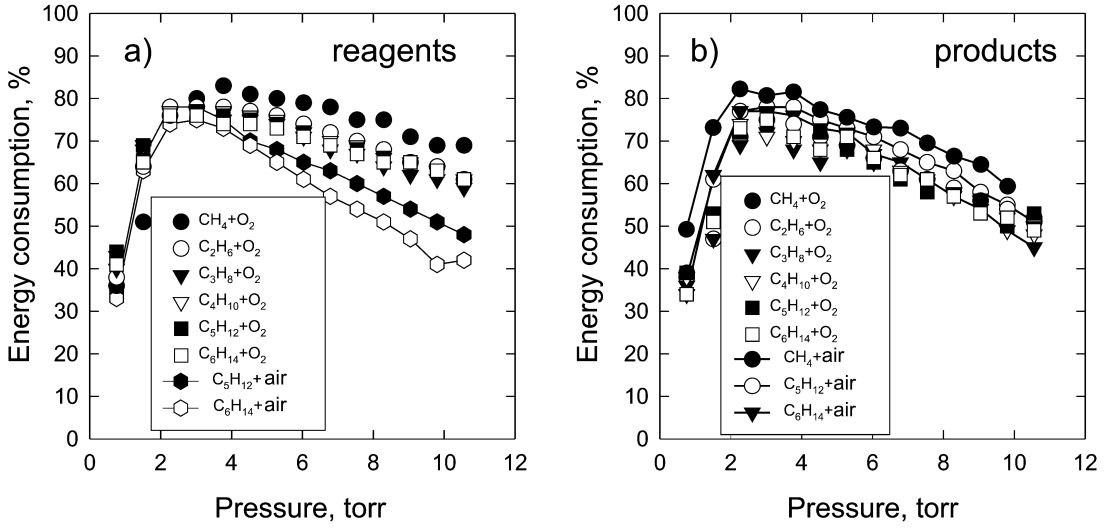

Fig. 4 The sum of energy input in the first and second high-voltage pulses: (a) in the initial mixture, (b) in the mixture transformed by the discharge.

Kinetics of alkane oxidation in the discharge

The emission spectra of the discharge in the pure methane and in the processed methane–oxygen stoichiometric mixture are represented in Fig. 5. The spectrum in pure methane consists of a repulsive continuum of hydrogen (the transition $H_2(a^3\Pi - b^3\Sigma)$). The emission band of $CH(A^2\Delta \rightarrow X^2\Pi)$, which corresponds to the transition $v' = 0 \rightarrow v'' = 0$, is well identified. The main part of the molecular bands of visible and near ultraviolet ranges, which appears in the processed methane–oxygen mixture, belongs to the molecule $CO_2^+(A^2\Pi)$. The bands of the radical $OH(A^2\Sigma \rightarrow X^2\Pi)$ can be definitely identified. We can identify and control some weak bands of CO Angstrom system ($CO(B^1\Sigma \rightarrow A^1\Pi)$).

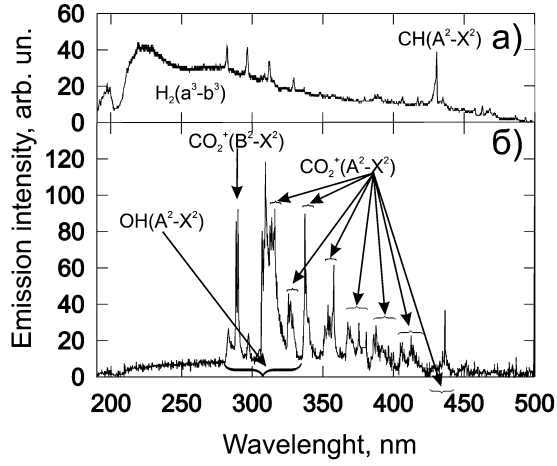

Fig. 5 Spectrum of discharge emission (a) in pure methane and (b) in the processed methane–oxygen mixture. The pressure is 4 Torr.

From Fig. 5, it is clearly seen that the CH($A^2\Delta \rightarrow X^2\Pi$) band emission in methane is strongly overlapped by CO_2^+($A^2\Pi \rightarrow X^2\Pi$) in the mixture. Hence, at the early stage of methane–oxygen mixture processing, it is important to take the necessary steps to separate these bands. The OH($A^2\Sigma \rightarrow X^2\Pi$) spectrum is also overlapped by the CO_2^+ emission spectrum. In mixtures of alkanes with air, there appear to be multiple and strong bands of 1st negative and 1st and 2nd positive systems of nitrogen in the spectrum. They partially overlap the emission spectrum of CH, CO_2^+, and OH bands. In the Angstrom system, the band at 518.6 nm is not overlapped by other bands. In all the experiments weak lines of the Balmer series of hydrogen were observed.

As indicated above, when the spectra overlapped, molecular bands were identified on the basis of the time-resolved experiments. The listed bands of the molecules were registered in all investigated stoichiometric mixtures, both in mixtures with oxygen and with air, and these bands were used as indicators of hydrocarbon oxidation process in the discharge.

Taking into account the quenching rate constants and the lifetime of these states, measured in time-resolved experiments (the method is described in detail in [8]), the excitation rates of emitting states integrated over the discharge time were reconstructed. It is worth noting that the quenching rate constants of ions CO_2^+($B^2\Sigma$), CO_2^+($A^2\Pi$), and N_2^+($B^2\Sigma$) by reagents and products practically do not differ. On the contrary, the quenching rate constants of CO($B^1\Sigma$), CH($A^2\Delta$), and OH($A^2\Sigma$) states are approximately 30–50 % higher in products than these in reagents. This fact can be explained by the appearance of water in the products.

In stoichiometric mixtures of alkanes with air, the excitation rates of N_2($C^3\Pi$, $v' = 1$), N^2($B^3\Pi$, $v' = 6$), and N_2^+($B^2\Sigma$, $v' = 0$) have been obtained on the basis of the time-resolved emission of transitions N_2($C^3\Pi$, $v' = 1 \rightarrow B^3\Pi$, $v'' = 7$), N_2($B^3\Pi$, $v' = 6 \rightarrow A^3\Sigma$, $v'' = 3$), and N_2^+($B^2\Sigma$, $v' = 0 \rightarrow X^2\Sigma$, $v'' = 2$). These rates were obtained at the instant of time when the discharge was switched on and after the oxidation was over. We integrated these rates over the time of the discharge. It has been shown that the integral rates at the instant of time corresponding to the discharge start do not change until the moment the oxidation is over. During the process of oxidation, the rate of N_2^+($B^2\Sigma$, $v' = 0$) state excitation decreases by 25 % approximately. Paper [8] under similar condition has shown that N_2($C^3\Pi$, $v' = 1$) and N_2^+($B^2\Sigma$, $v' = 0$) states are excited by a direct electron impact from the ground state of molecular nitrogen. Since in the discharge the nitrogen concentration is practically constant, then the integral rate constants of N_2($C^3\Pi$, $v' = 1$) and N_2^+($B^2\Sigma$, $v' = 0$) states excitation change in the process of oxidation by 10 and 25 %, correspondingly. We noted that the excitation of N_2($C^3\Pi$, $v' = 1$) and N_2^+($B^2\Sigma$, $v' = 0$) takes place during the high-voltage pulses, at the same time N_2($B^3\Pi$, $v' = 6$) is generally excited in the discharge afterglow and its excitation rate correlates with the emission of N_2($C^3\Pi$, $v' = 1 \rightarrow B^3\Pi$, $v'' = 7$) transition. Therefore, we can conclude that the N_2($B^3\Pi$, $v' = 6$) state is excited in the deactivation processes of the N_2($C^3\Pi$) state.

The excitation thresholds of N_2($C^3\Pi$, $v' = 1$) and N_2^+($B^2\Sigma$, $v' = 0$) states by electron impact are equal to ~12 and 19 eV, correspondingly. Inasmuch as the thresholds of all the investigated states are lower than 19 eV, it can be assumed that the rate constants of excitation of these electronic states integrated over the discharge emission time did not change by more than 25 % during the oxidation process. At the same time, the lower the threshold the smaller the change of the rate constant in the oxidation process.

Thus, the changes of the mixture composition in the oxidation process are caused by changes of quenching and excitation rates. Hence, on the basis of the integral emission intensity we can obtain qualitative dependencies of ground-state concentrations, which produce the excited states. At the same time, this fact slightly affects the characteristic time obtained from the integral emission of transitions CO($B^1\Sigma \rightarrow A^1\Pi$), CO_2^+($B^2\Sigma \rightarrow X^2\Pi$), OH($A^2\Sigma \rightarrow X^2\Pi$), and CH($A^2\Delta \rightarrow X^2\Pi$).

The dependencies between the integral intensity of the emission and the time in the methane mixtures were approximated by the function $\exp(-t/\tau(p))$ or the function $1 - \exp(-t/\tau(p))$ with good accuracy (see Fig. 6). It is necessary to note that during the experiment the full oxidation of methane was

registered that is clearly proven by the $[CH_4](t)$ curve obtained from the laser absorption measurements in Fig. 6. Here, the integral emission of $CH(A^2\Delta \rightarrow X^2\Pi)$ radical is shown. It is clearly seen that the emission intensity profile of $CH(A^2\Delta \rightarrow X^2\Pi)$ does not differ from the methane concentration curve. This fact allows us to assume that the $CH(A^2\Delta \rightarrow X^2\Pi)$ emission is a good indicator of hydrocarbons in the discharge.

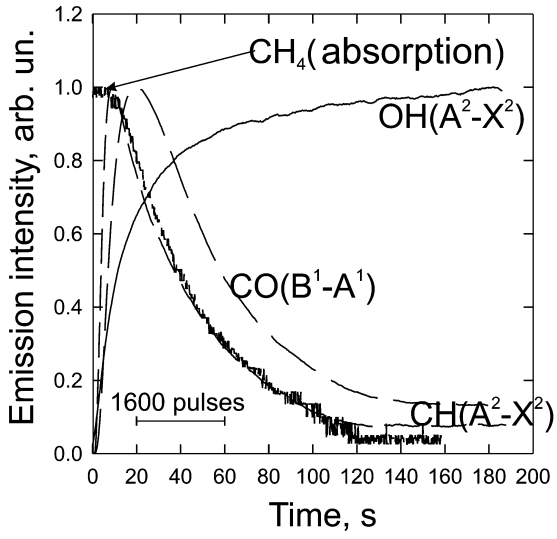

Fig. 6 Integral over time emission intensities of transitions $CH(A^2\Delta \rightarrow X^2\Pi)$, $CO(B^1\Sigma \rightarrow A^1\Pi)$, $OH(A^2\Sigma \rightarrow X^2\Pi)$, and methane concentration measured by absorption of He–Ne laser emission on the wavelength $\lambda = 3.3922$ μm in the discharge. The initial pressure of the mixture $CH_4 + O_2$ is 7.56 Torr.

In the mixtures of alkanes, which are much heavier than methane, the emission dependencies exhibit a more comprehensive form that can be explained by accumulation of intermediates (probably CO and unsaturated hydrocarbons) in the alkane oxidation process and the following after-oxidation. The example of integral oxidation of the ethane under 7.54 Torr pressure is presented in Fig. 7. It is obvious that the curves are not described by simple functions and essentially differ from each other.

The time of complete oxidation is defined as the time when the signal from the photomultiplier reaches the level of $0.95I_\infty$ for the wavelengths (290 and 307.8 nm) corresponding to $OH(A^2\Sigma \rightarrow X^2\Pi)$ and $CO(B^1\Sigma \rightarrow A^1\Pi)$ transition and the level $1.05I_\infty$ for the wavelengths (430 and 518.6 nm) corresponding to $CO_2{}^+(B^2\Sigma \rightarrow X^2\Pi)$ and $CH(A^2\Delta \rightarrow X^2\Pi)$ transitions.

It is important to note that the oxidation times obtained from the emission of different bands under the same experimental conditions are rather different owing to the different influence of the excitation processes and quenching at different states during the mixture transformation, but the times obtained from the emission of the same band in different mixtures are practically the same and are within the experimental accuracy. Because of the fact that the experimental dispersion is minimal for the time obtained from $CO(B^1\Sigma \rightarrow A^1\Pi)$ band emission, we designate the time obtained from the emission of this band as the time of alkane full oxidation.

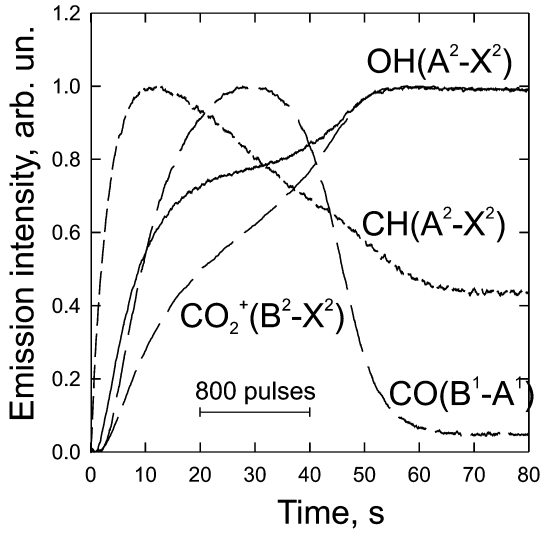

Fig. 7 Integral over time emission intensities of transitions CH($A^2\Delta \rightarrow X^2\Pi$), CO($B^1\Sigma \rightarrow A^1\Pi$), CO_2^+($B^2\Sigma \rightarrow X^2\Pi$), and OH($A^2\Sigma \rightarrow X^2\Pi$) in the discharge. The initial pressure of the mixture $C_2H_6 + O_2$ is 7.56 Torr.

Figure 8 presents the times of complete oxidation for different alkanes. It is clearly seen that the time of complete methane oxidation is nearly twice as large as the times of complete oxidation for other alkanes, both for the mixtures with oxygen and the mixtures with air. For other alkanes, the times of complete oxidation do not differ. In the mixture with air, the times of complete oxidation are twice or more as short as the times in the similar mixtures with oxygen. Taking into account that the total quantity of alkanes is smaller in the stoichiometric mixtures with air than that in the mixtures with oxygen, the oxidation rates of alkanes in the mixtures with oxygen are twice as small as those in the mixtures with air.

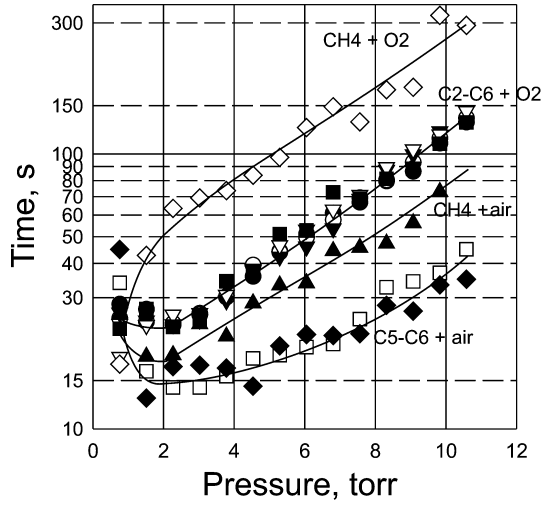

Fig. 8 Dependencies between alkanes full oxidation times and initial pressures of stoichiometric mixtures, obtained from CO($B^1\Sigma \rightarrow A^1\Pi$) band emission. The data for the stoichiometric mixtures of oxygen with alkanes from ethane to hexane are denoted as $C_2H_6 + O_2$, and data for the stoichiometric mixtures of oxygen with alkanes from ethane to hexane are denoted as C_5C_6 + air (see Table 1).

Thus, the stoichiometric mixtures of alkanes with air and oxygen under the action of nanosecond uniform discharge have been oxidized completely at ambient temperature. The time necessary for oxidation of all alkanes starting from ethane is equal for all stoichiometric mixtures. The methane is oxidized twice slower than any other investigated alkane.

C_4H_{10} oxidation in lean mixtures with oxygen under nanosecond discharge

As indicated above, oxidation of alkanes starting from ethane under the action of nanosecond discharge proceeds for the same time under the same experimental conditions (initial pressure, energy input). One can explain this fact using the assumption of weak influence of excited and charged particles produced by an electron impact on hydrocarbon molecules, the main influence here being the electron impact on oxygen, intermediates, and products (especially, water).

It is known that the electron impact dissociation thresholds of alkanes (in a methane–propane set) reduce approximately on 1 eV per additional carbon's atom in the molecule. The steric factor increases proportionally to the quantity of C atoms in an alkane molecule, at the same time the concentration of alkane in the stoichiometric mixture decreases inversely proportional to the quantity of C atom. Thus, it should be expected that when changing the stoichiometric mixtures from light to heavy alkanes, the variation of the alkane concentration will be compensated by a variation of the steric factor. However, when the quantity of carbon's atom in an alkane molecule increases, the dissociation threshold by electron impact decreases. Of course, a faster oxidation of the heavier alkanes should be expected in comparison with lighter ones, which were not obtained in the experiments.

The time of complete oxidation obtained from CO($B^1\Sigma \rightarrow A^1\Pi$) integral emission and the time of the maximum of CO($B^1\Sigma \rightarrow A^1\Pi$) emission are presented in Fig. 9. It is clearly seen that the time decreases linearly with decreasing of the equivalence ratio, which should be expected in the case of weak influence of excitation, dissociation, and ionization of alkanes by the electron impact. Really, the quantity of oxygen in stoichiometric mixture differs from that in the mixture with equivalence ratio of 0.1 by 11 % only. Thus, the variation of concentration of excited molecules, ions, and atoms of oxygen is less than 11 % compared to the stoichiometric mixture case. At the same time, the concentration of butane changes by an order of magnitude, therefore, the dependence between the time of complete oxidation and the equivalence ratio have to be linear with good accuracy.

Thus, under our experimental conditions, the excitation, ionization, and dissociation of an alkane by electron impact did not influence the rate of the alkane oxidation. The oxidation process is controlled by the processes of producing ions, excited molecules, and atoms from oxygen during the first stage of the process, and water and carbon dioxide during the last stage of hydrocarbon oxidation.

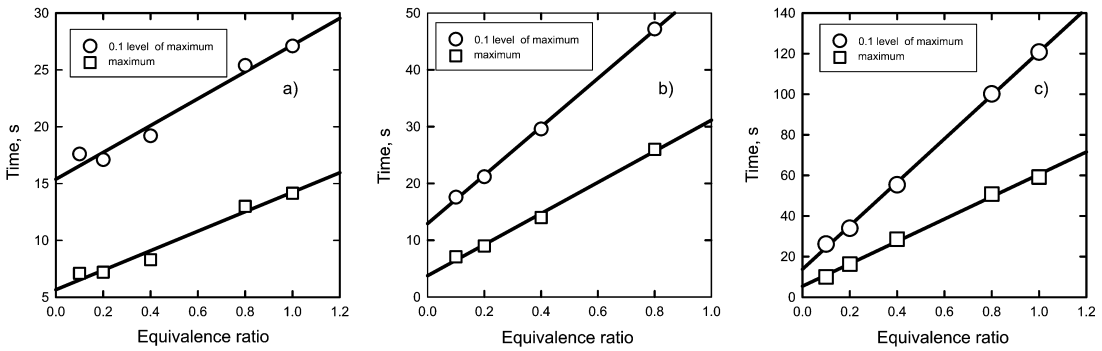

Fig. 9 Time of full oxidation obtained from CO($B^1\Sigma \rightarrow A^1\Pi$) band emission and time of CO($B^1\Sigma \rightarrow A^1\Pi$) band emission maximum vs. initial pressure of butane with oxygen lean mixtures. (a) p = 2 Torr, (b) p = 6 Torr, (c) p = 10 Torr.

$C_{10}H_{22}$ oxidation in lean mixture with oxygen under the action of nanosecond discharge

Real fuels used in internal-combustion engines consist of hydrocarbons C_8–C_{16}, therefore, the universality of the above conclusions should be proved on the example of an alkane higher than C_6. For this we have chosen an *n*-decane $C_{10}H_{22}$.

At 25 °C, pressure of saturated vapor of *n*-decane is equal to 0.9 Torr, which corresponds to 18 Torr of the maximal pressure of the stoichiometric mixture with oxygen. Preparation of the mixture was similar to hexane and pentane mixtures. A portion of decane was injected into the 10-liter vacuum-processed volume. The portion of decane was smaller than the value of the saturated vapor pressure of *n*-decane at 25 °C in a 10-liter vessel. Later, we added some oxygen into the vessel. The mixture was stirred by a ventilator. In spite of the forced mixing, the concentration of decane increased very slowly, which we explained by very slow evaporation of decane under ambient temperature.

The emission intensity of $OH(A^2\Sigma \rightarrow X^2\Pi)$ in the processed stoichiometric mixture of butane with oxygen was used as a reference curve. We controlled the concentration of decane by the following method. The current mixture was oxidized in a nanosecond discharge.

The spectrum of emission of the mixture was compared with the spectra obtained in the processed mixtures of butane and oxygen with a different equivalence ratio.

Emission intensities of OH and CO_2^+ bands in the oxidation products of butane–oxygen mixtures of different composition essentially nonlinearly depend on the equivalence ratio.

We explained this fact by the influence of water concentration on the electron energy distribution function, that is, by the changes of the constants of excitation of these states by the electron impact with water concentration changes. Figure 8 also presents the emission intensities of the processed decane oxygen mixture on the same wavelengths. The emission intensities of different bands were interpolated among the measured points and linearly extrapolated to the zero point. These dependencies allowed us to obtain the equivalence ratio of the decane mixture. The values of the equivalence ratio determined from the measurements performed on different wavelengths and in different pressures are presented in Table 3.

Table 3 Equivalence ratio values.

Pressure, Torr	1.51	5.29	9.83
λ = 290 nm	0.096	0.116	0.08
λ = 306 nm	0.205	0.114	0.135
λ = 330 nm	0.12	0.129	0.113

Thus, we investigated the oxidation process in the mixture with 0.12 ± 0.01 stoichiometric ratio. The energy contribution and $CO(B^1\Sigma \rightarrow A^1\Pi)$ emission intensity were registered. The energy contribution depending on the pressure is presented in Fig. 10 for both the decane and butane mixtures. It is necessary to note that the difference between the energy inputs in initial and processed mixtures is negligibly small, owing to oxygen being the main constituent of these mixtures.

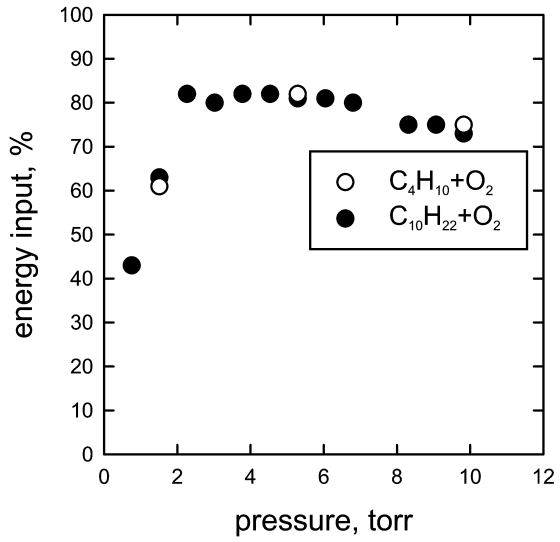

Fig. 10 Energy input for butane and decane mixtures with O_2. Equivalence ratio of butane mixture is 0.1, and one of the decane mixtures is 0.12 ± 0.01.

It is clearly seen that the energy contribution in different mixtures does not differ within the range of the experimental errors. Thus, gas excitation occurred with the same intensity in all mixtures.

Figure 11 displays the times of complete oxidation obtained by emission intensities of $CO(B^1\Sigma \rightarrow A^1\Pi)$ bands for butane–oxygen and decane–oxygen mixtures. It is clearly seen that the time of complete oxidation of *n*-decane is approximately equal to the time of complete oxidation of butane in mixture with 0.1 equivalence ratio. Thus, the conclusions we made earlier for the mixtures of alkanes C_2–C_6 can be assigned to alkanes that are heavier.

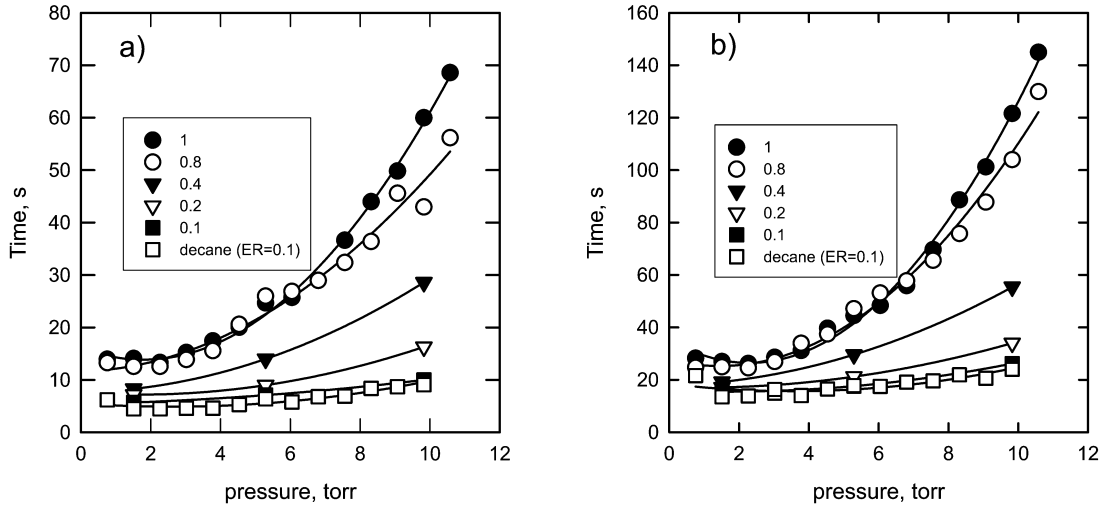

Fig. 11 Time intervals between discharge start and $CO(B^1\Sigma \rightarrow A^1\Pi)$ emission maximum (a) and instants of full oxidation (b).

CONTROL OF COMBUSTION AND IGNITION OF HYDROCARBON-CONTAINING MIXTURES BY NANOSECOND PULSED DISCHARGES

Control of flame propagation

The main part of the experimental set-up is a quartz nozzle with rectangular section. Three different nozzles, with 2.2, 2.5, and 4.3 mm in width and the same length of 30 mm, were investigated. A stainless-steel 0.8-mm-thick high-voltage electrode was placed inside the nozzle, and the grounded electrodes were situated near the nozzle edges, parallel to them. In order to prevent a transition of the discharge into a spark form, they were set tightly into quartz tubes. On applying a voltage to the gap, a barrier discharge occurred, so the maximum possible current was limited by the dielectric. A more detailed description of the set-up can be found in [9].

To fix the point of streamer start and the number of streamers as well, the high-voltage electrode has a number of pins on its upper edge. Two electrodes were used, with 8 and 15 pins, so the number of streamers could be 16 or 30, respectively. The nozzle and images of discharge and flame are presented in Fig. 12.

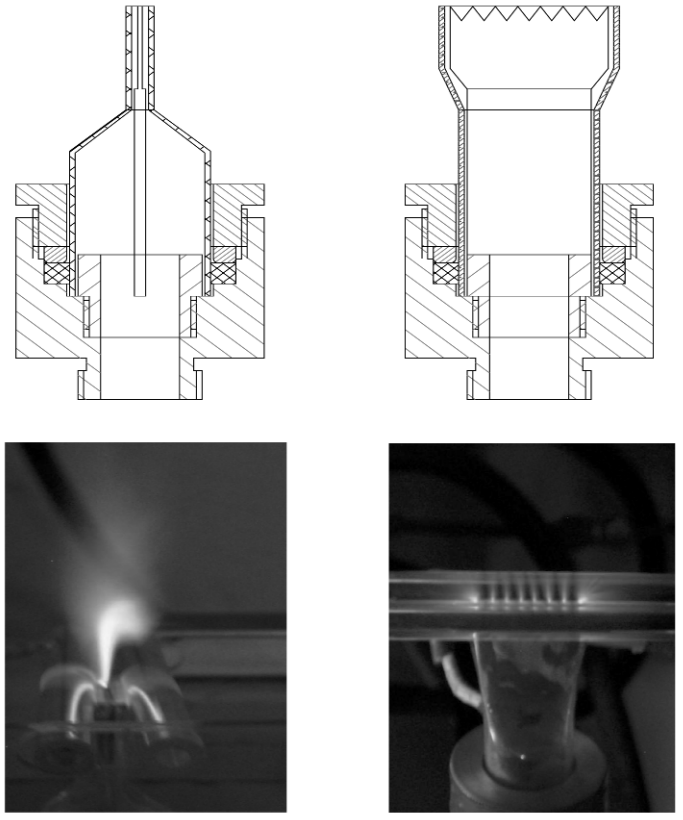

Fig. 12 Quartz nozzle and discharge view.

Earlier, it was shown by the authors in [9] by picosecond intensified charge-couple device (ICCD) camera images that the energy inputs in the mixture only during the first 10–20 ns of pulse duration, and then the region of energy release moves beyond the zone of mixture flow and is situated near the grounded electrodes. To increase the effectiveness of energy input, the principal scheme of high-voltage generator (HVG) has been changed entirely. Instead of a rotation interruptor scheme with pulses of

77 ns full width half-maximum (FWHM), we used the idea of magnetic compression to reduce the pulse length. In the present work, we used three different types of pulses: with FWHM 7, 19, and 24 ns. The voltage on the discharge gap could be 14 or 22 kV, the nanosecond pulse polarity was positive. The pulse repetition rate could be varied within the range of 400–1000 Hz.

The investigations of active particle production were performed by emission spectroscopy methods. The recording facility consisted of CCD-line (spectral range of λ = 200–800 nm) and MDR-41 monochromator (with an operating range of λ = 190–600 nm and a linear dispersion of 0.96 nm/mm). The optical system was calibrated using a standard emission source (a calibrated DDS-30 deuterium arc lamp emitting in the range 190–500 nm).

It was shown in [1] that active particles (such as O, H, OH, and so on) responsible for chain branching play the main role in processes of combustion acceleration and flame velocity increase.

Production of additional centers results in acceleration of chemical kinetic processes. A proper organization of energy input is another important feature. The energy should be injected into the gap that will lead to radical production rather than gas ionization or thermal heating. A streamer type of discharge satisfies these conditions completely. The main area, where the active particles are produced, is the streamer head which is quite small (~0.05 cm for typical voltages of 10–20 kV [10]), but the values of reduced electric fields in the ionization wave front (up to 800 Td) are rather high.

Influence of high-voltage pulse duration

We have just shown that if we are making the pulse shorter (24 vs. 77 ns in the previous work [9]), we can increase the efficiency of the energy input (we have reduced the energy input more than 2 times and still have the same increase in the flame blow-off velocity). But the pulse should be longer than the time of the streamer propagation through the gap where the mixture is flowing, to provide a full overlapping of the nozzle by the streamer. The streamer velocity was calculated in [10] and is equal to 0.6 mm/ns under the voltage of 22 kV, so in the case of 14 kV, as in our experiment, the velocity value is even lower.

A number of experiments have been performed with pulses of different duration. Two types of additional line pieces were used to provide different pulse duration (FWHM 7 and 19 ns). It was found that at frequency 500 Hz and ER = 0.8, the 19 ns pulse is much more efficient than the 7 ns one for all the three nozzles and the advantage of using 19 ns grows with nozzle widening (Fig. 13), as it was predicted earlier.

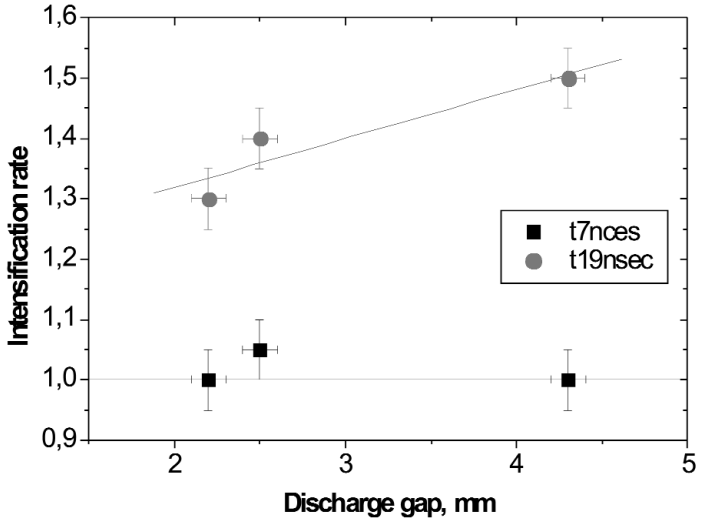

Fig. 13 Discharge influence on flame blow-off velocity for different pulse durations.

Kinetics of the flame acceleration

A series of experiments have been carried out to prove the correctness of the model of flame acceleration and kinetic scheme suggested in the previous work [9]. That is why it is very important to make spectroscopic investigations of the flame itself and the flame under discharge. In [9], the profile of OH radical along the height above the burner (HaB) in propane-air flame was presented. That result was based on the nonresolved spectrum (OH($A^2\Sigma$, $v' = 0 \rightarrow X^2\Pi$, $v'' = 0$)) at 306.4 nm with quite a large apparatus function of monochromator (2.4 nm). This caused a question: Is the first peak of the typical "two-humped" spectrum connected with N_2 production in the discharge? The second positive system of nitrogen $C^3\Pi_u \rightarrow B^3\Pi_g$ has intense lines on the wavelengths of 315.9 nm ($1 \rightarrow 0$), 313.6 nm ($2 \rightarrow 1$), and 311.6 ($3 \rightarrow 2$). In the present work, using a CCD-array with the signal accumulation mode (50 °C up to 30 min exposure time), it became possible to obtain a rotationally resolved spectrum of OH radical in methane–air flame. The spectra of OH* for two different heights (0 and 6 mm) above the burner are presented in Fig. 14. It is distinctly seen that in the region below 310–312 nm we can use any rotational line of OH* spectrum to build the dependence between OH* emission and the HaB. The result is presented in Fig. 15 and this figure confirms the previously obtained results for the propane–air mixture as well as the importance of OH radical in flame and the similarity of kinetic processes which lead to a flame blow-off velocity increase for the vast majority of premixed hydrocarbon–air flames. The results for methane–air flame blow-off velocity increase (Fig. 16) are in agreement with this theory.

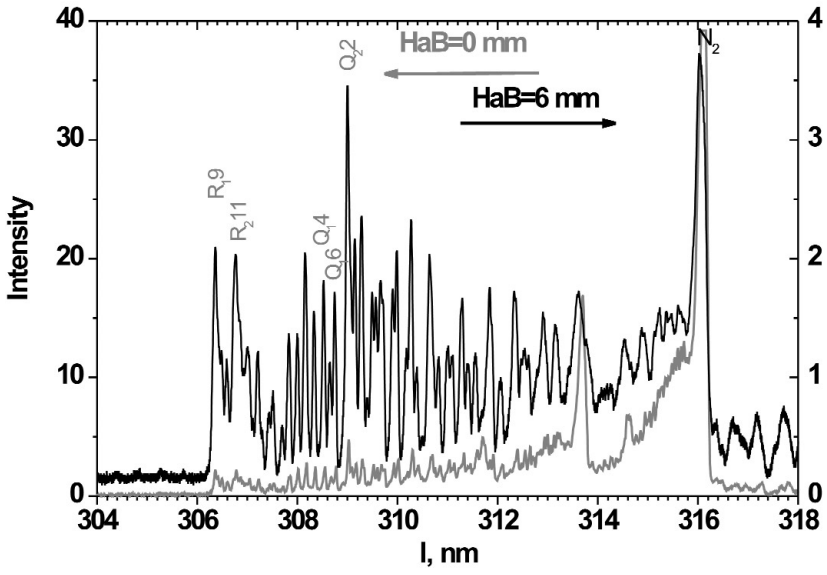

Fig. 14 OH* spectra in methane–air flame under discharge action at HaB = 0 mm and HaB = 6 mm.

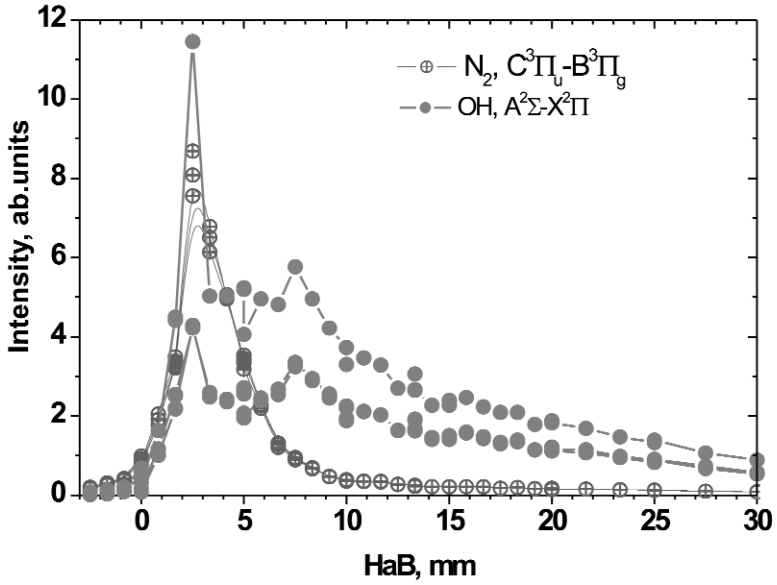

Fig. 15 OH* profile along the HaB in methane–air flame.

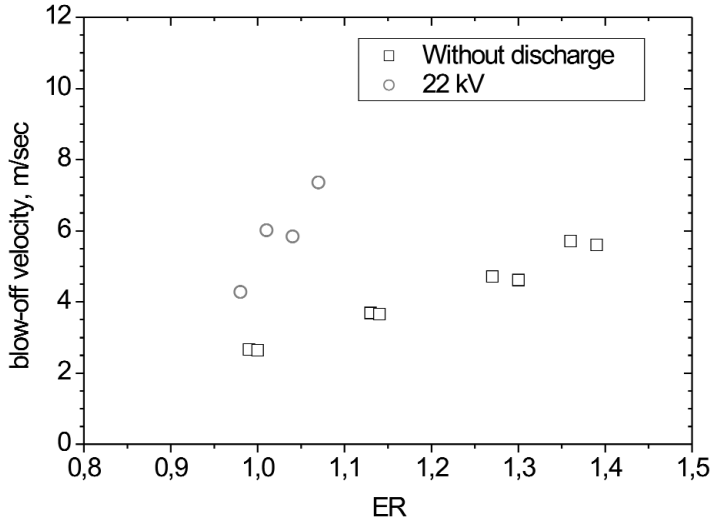

Fig. 16 Methane–air flame blow-off velocity increase.

Temperature gradient in the flame front

The rotational temperature was calculated using OH rotationally resolved spectra. The technique of temperature determination is described in [11]. We used the ratio of $R_1(9)$ (λ = 306.3565 nm) line and $Q_1(4)$ (λ = 308.3278 nm) line. In case of an equilibrium flame, the rotational temperature obtained in such a way is close to the translational temperature (the radiative time of living of $A^2\Sigma$ level is 690 ns [12], and the typical time between particles collisions is about 1 ns, so the Boltzmann distribution of particles at rotational levels occurs before radiation). The experimental OH rotational temperature profiles along the HaB in methane–air flame are presented in Fig. 17.

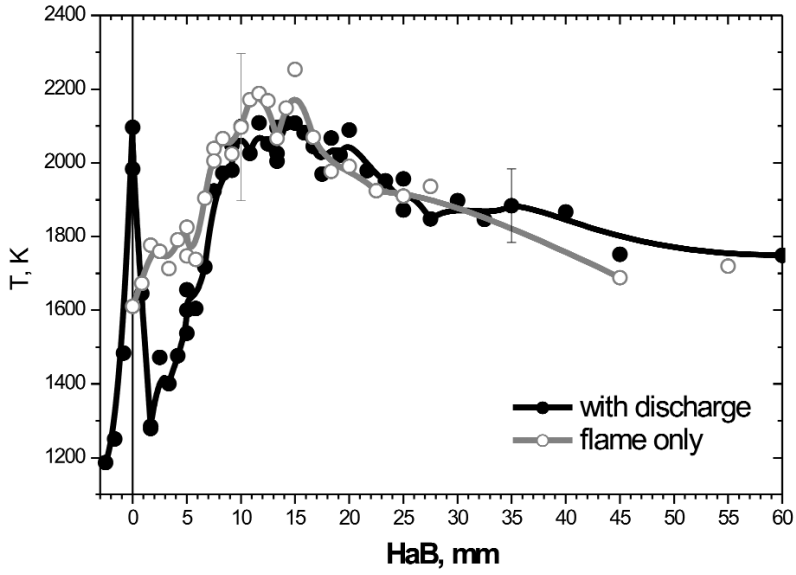

Fig. 17 Experimental OH rotational temperature profile along the HaB in methane–air flame.

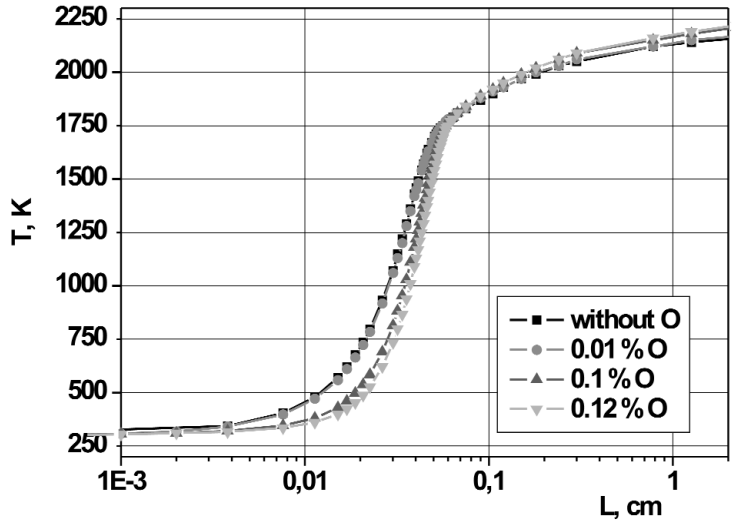

Fig. 18 Calculated temperature profile along the HaB in methane–air flame.

The comparison of the experimental profile with the calculated one (Fig. 18) shows a good data agreement. The theoretical model is based on changing in the composition of the initial mixture under the discharge action.

The main channel of O and OH production is the quenching of electronically excited triplet states of N_2 on the oxygen molecules in the processes:

$$N_2\left(A^3\Sigma_u^+\right) + O_2 \rightarrow N_2\left(X^1\Sigma_g^+\right) + O + O \quad (1)$$

$$N_2\left(B^3\Pi_g\right) + O_2 \rightarrow N_2\left(X^1\Sigma_g^+\right) + O + O \quad (2)$$

$$N_2\left(C^3\Pi_u\right)+O_2 \rightarrow N_2\left(X^1\Sigma_u^+\right)+O+O \tag{3}$$

$$N_2\left(a'^1\Pi_g\right)+O_2 \rightarrow N_2\left(X^1\Sigma_u^+\right)+O+O \tag{4}$$

or dissociation of oxygen molecule which can proceed through its electronically excited states:

$$O_2\left(\text{el.exc.}\right) \rightarrow O\left(^3P\right)+O\left(^3P\right) \tag{5}$$

$$O_2\left(\text{el.exc.}\right) \rightarrow O\left(^3P\right)+O\left(^1D\right) \tag{6}$$

Ignition by pulsed nanosecond discharge

The influence of nonequilibrium plasma pulsed discharge as an igniter of combustible mixtures at various pressures and temperatures has been investigated using the shock tube (ShT) technique [13]. The experiments were carried out behind a reflected shock wave as in classical experiments on the autoignition of combustible mixtures [14,15]. The experimental set-up (see Fig. 19) consisted of a ShT with a DC, a vacuum and gas supply system, a system for ignition by the discharge, and a diagnostic system. The ShT (25 × 25-mm square cross-section) had a 1.6-m-long work channel. The length of the high-pressure cell (HPC) was 60 cm. There were two pairs of windows for optical diagnostics along the stainless-steel working channel. The last section of the ShT with a 25 × 25-mm square cross-section was made from 40-mm-thick plexiglas and had eight optical windows (quartz and MgF_2). The metal endplate (EP) of the tube served as a high-voltage electrode. Another electrode was the grounded steel section of the ShT.

The nanosecond discharge was initiated at the instant when the reflected shock wave arrived at the observation point (point *A* in Fig. 19). High-voltage pulses were produced by a Marks-type HVG. At the output of the forming line, the voltage growth rate was about 80 kV/ns, which enabled the operation of the gas discharge in the form of an FIW in the dielectric section of the ShT. The velocity of the ionization wave front was 10^9–10^{10} cm/s, depending on the experimental parameters.

The diagnostic system consisted of a system for monitoring the shock wave parameters, a system for detecting ignition, a system for studying the spatial structure of the discharge and combustion, and a system for monitoring the electric parameters of the nanosecond discharge. The velocity of a shock wave was measured by the Schlieren system, which consisted of three He–Ne lasers and a set of photodiodes (PDs). The gas density (ρ_5), pressure (P_5), and temperature (T_5) behind the reflected shock wave were determined from the known initial gas mixture composition, the initial pressure, and the velocity of the incident shock wave. The ignition delay time was controlled using OH emission (λ = 306.4 nm, $A^2\Sigma(v' = 0)$ $X^2\Pi(v'' = 0)$ transition) in the microsecond time scale. Simultaneously, with this we controlled the emission from the discharge with the nanosecond time resolution, the current through the DC, and the voltage drop between the high-voltage electrode and the cross-section of the measurement.

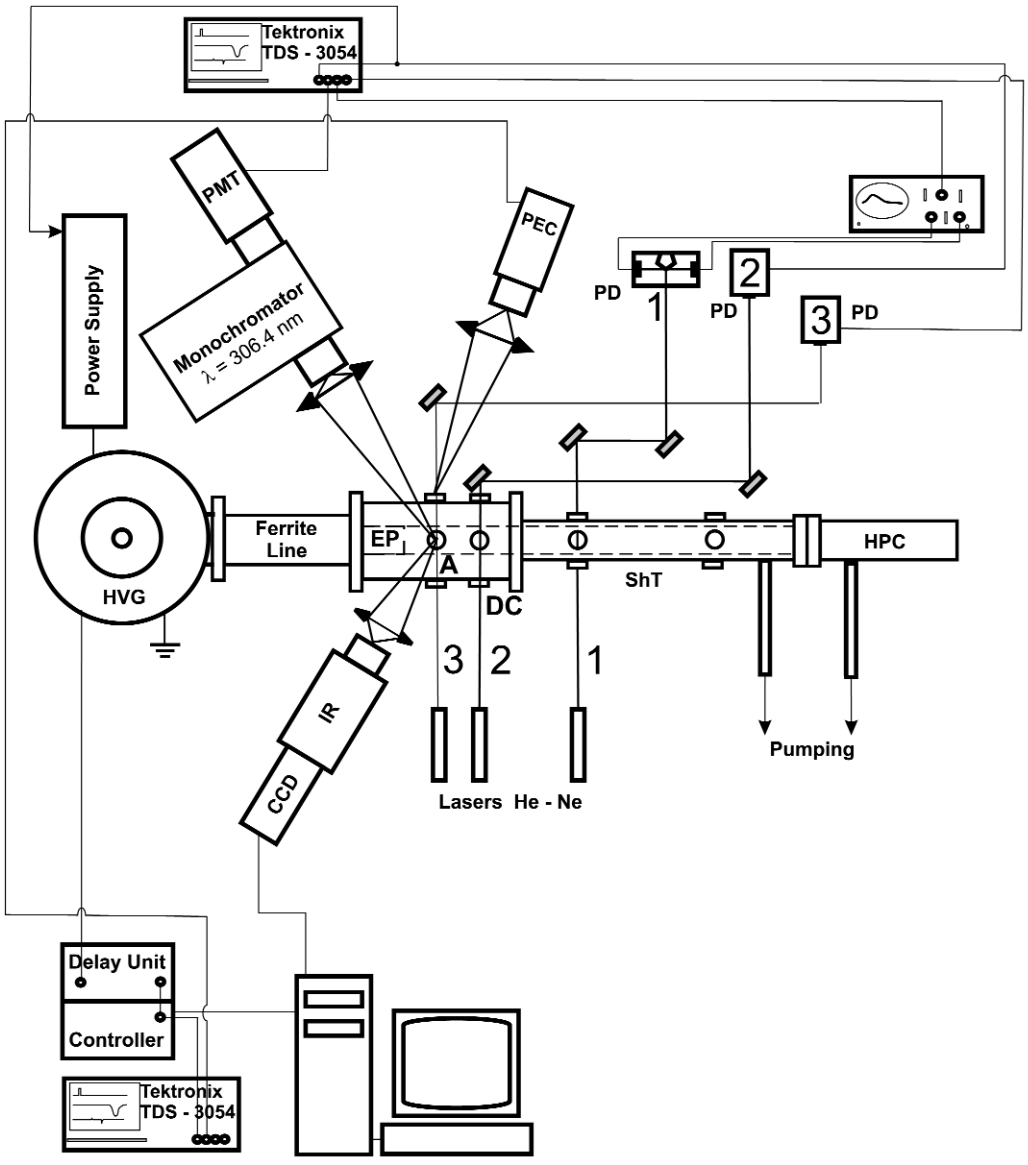

Fig. 19 Scheme of the experimental set-up. CCD: a cross-section of measurement, CCD camera; DC: discharge cell; EP: end plate; HPC: high-pressure cell; HVG: high-voltage generator; ShT: shock tube; PD: photodiode; PEC: photoelectric cell; PMT: photomultiplier.

Hydrocarbon–air mixture ignition by pulsed nanosecond discharge

As a reference result, we considered the data obtained for the methane-synthetic air stoichiometric mixture diluted by argon [16].

The question about efficiency of ignition of different hydrocarbons in homological series by the nanosecond discharge still remains open. This part of the paper is devoted to the results of the experimental investigation of the ignition delay under the action of a nanosecond discharge. The experiments were carried out using a set of stoichiometric mixtures C_xH_{2x+2}:O_2 (20 %) diluted by Ar (80 %) for hydrocarbons from CH_4 to C_4H_{10}. The temperature behind the reflected shock wave (T_5) varied from

980 to 1630 K, and the pressure (P_5) was from 0.17 to 1.0 atm. The composition of investigated mixtures is presented in Table 4.

Table 4 Investigated mixtures.

Alkane	CH_4	C_2H_6	C_3H_8	C_4H_{10}
	6.7 %	4.4 %	3.3 %	2.7 %
O_2	13.3 %	15.6 %	16.7 %	17.3 %
Air	80 %	80 %	80 %	80 %

The greatest change in OH emission intensity was observed for the methane–oxygen mixture diluted by argon. This is shown in Fig. 20. For the conditions of this pair of experiments, Schlieren signals are practically the same, but the discharge (indicated by a vertical line in the figure) shifts the ignition delay by hundreds of microseconds. The same effect, but less pronounced, is observed for all series of hydrocarbons. The difference in emission with and without discharge is presented, as an example, for butane–oxygen mixture, too (see Fig. 21).

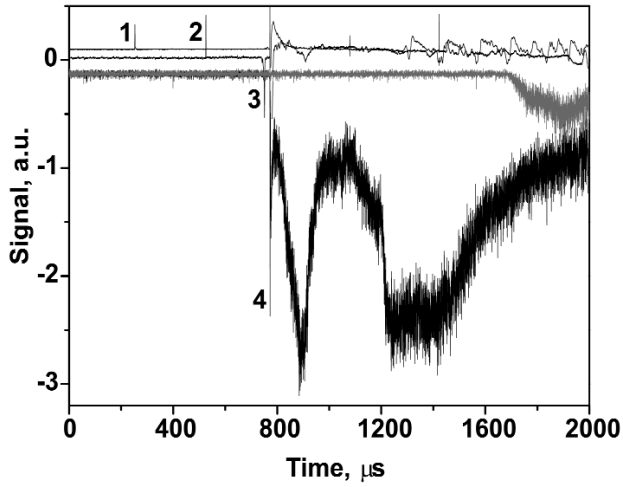

Fig. 20 Typical oscillograms from Schlieren detectors (upper curves) and from photomultiplier (two lower curves). Methane-containing mixture. 1,2: direct shock wave; 3: reflected shock wave; 4: discharge. Upper curve from photomultiplier corresponds to autoignition, lower one to ignition by FIW.

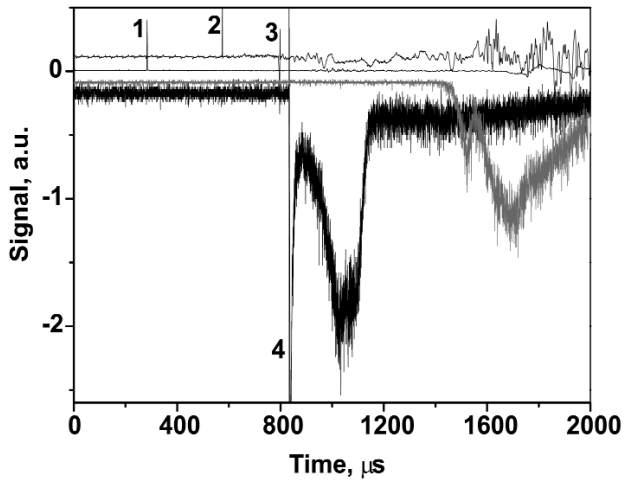

Fig. 21 Typical oscillograms from Schlieren detectors (upper curves) and from photomultiplier (two lower curves). Butane-containing mixture. 1,2: direct shock wave; 3: reflected shock wave; 4: discharge. Upper curve from photomultiplier corresponds to autoignition, lower one to ignition by FIW.

Figures 22–25 demonstrate the dependence between the ignition delay time for autoignition and ignition by nanosecond discharge for all the investigated mixtures. It is clearly seen that the ignition delay is well pronounced in all the cases. The difference for C_4H_{10} is the strongest in the region of 1100–1200 K, while for C_3H_8 the difference is practically constant within a range of 1400–1600 K and is about 200 K.

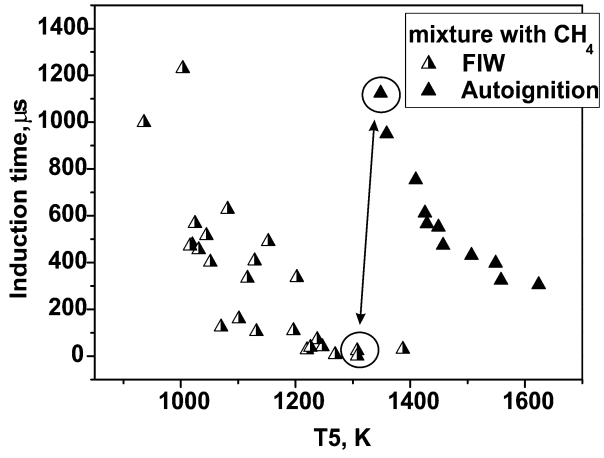

Fig. 22 Ignition delay time vs. temperature for methane-containing mixture.

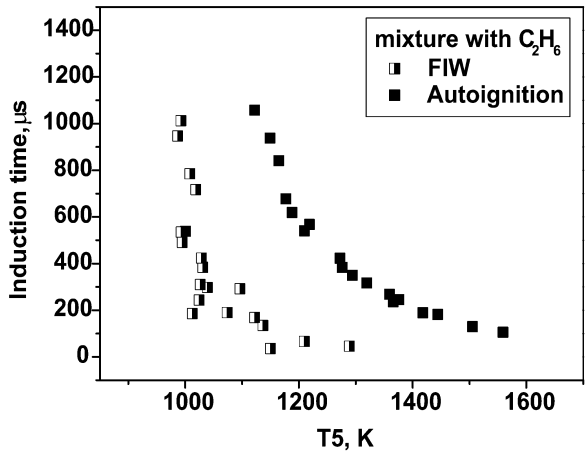

Fig. 23 Ignition delay time vs. temperature for ethane-containing mixture.

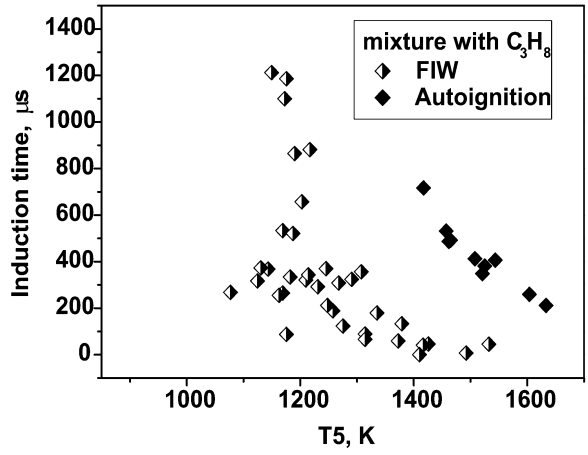

Fig. 24 Ignition delay time vs. temperature for propane-containing mixture.

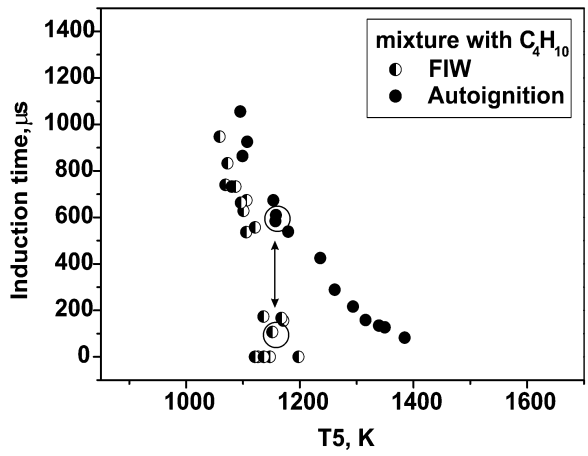

Fig. 25 Ignition delay time vs. temperature for butane-containing mixture.

Energy input measurements

Energy measurements have been performed for different mixtures. The results are demonstrated in Fig. 26. It is obvious that the energy values are of the same order of magnitude as in the methane-containing mixture. This is quite clear because for a mixture with 80 % of Ar dilution and 13–17 % of O_2, the energy input into the discharge is determined mainly by Ar and O_2. It is seen from the figure, that the main part of the experimental points is within the interval 7–13 mJ/cm^3 (this region is separated by two horizontal lines).

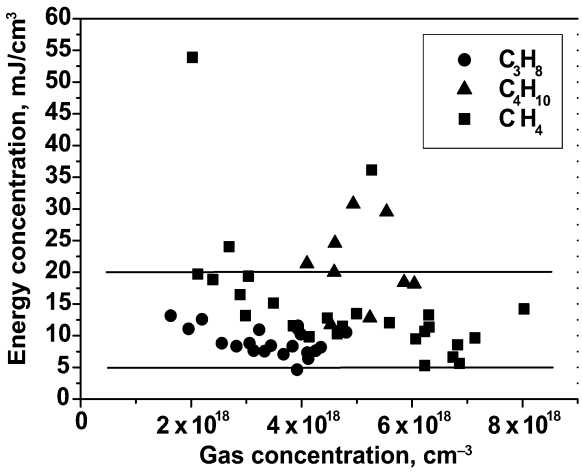

Fig. 26 Energy input into discharge for different gases.

PLASMA-ASSISTED DEFLAGRATION-TO-DETONATION TRANSITION

The most popular method of a run-up distance reduction is application of different types of obstacles, which disturb the flow and increase the flame velocity [17–22]. The modification of this method is an application of a two-chamber initiating system where the mixture is ignited in the first chamber but the detonation wave is initiated in the other chamber [20–22]. In this case, acceleration of the flame front depends on its own speed and strength. If the velocity of the flame front is low, the turbulization and consequent acceleration of the flame are weak. Usually, the initial flame front is weak, so this method is not very effective. It is possible to avoid the above disadvantage using a gradient mechanism [23]. The high-voltage nanosecond discharge allows us to produce active species in the bulk volume. The required gradient of active species is created by the geometry of the DC. In this way, the high-voltage nanosecond discharge allows us to reduce the length of DDT.

A number of scientific groups carried out investigations of ignition by corona discharges [24,25]. The experiments have been performed for ethylene–air, methane–air [24], and propane–air [25] mixtures. The authors have applied the pulse nanosecond discharge with duration of 50 ns. They have compared the ignition delay times under ignition by the corona and by the conventional spark discharge with the same energy. The ignition delay time is shorter by a factor 3–5 under ignition by the pulse corona discharge as compared to thermal ignition.

The experimental set-up is shown in Fig. 27. The experiments were performed in a detonation tube with the diameter of 140 mm. The discharge device was attached to the end plate of the detonation tube. The discharge chamber consists of 131 separated sections, which have common high-voltage and grounded electrodes. The discharge device provides uniform excitation at the length of 80 mm. The discharge chamber and the detonation tube are separated by an orifice plate. The orifices are arranged opposite to each electrode. In the experiments, the high-voltage electrodes were supplied with a positive

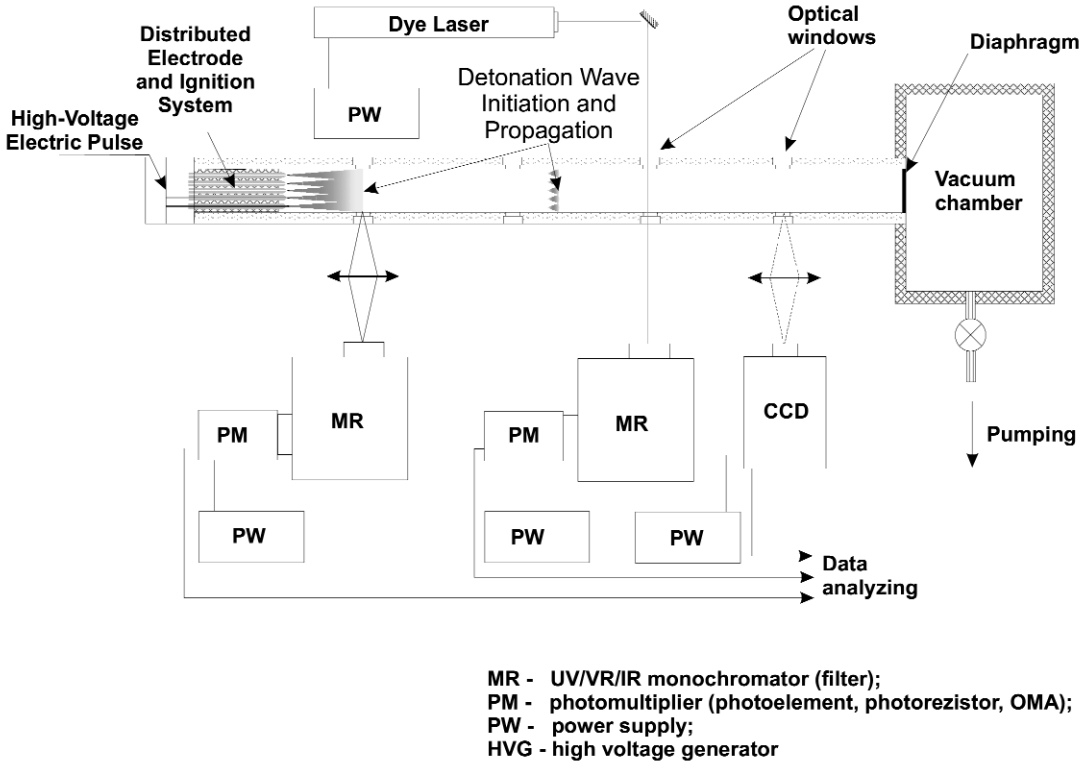

Fig. 27 Scheme of experimental set-up for DDT investigations.

pulse with the amplitude of 4–70 kV and the duration at the half-width of 50 ns. The calculated reduced electric field ranges from 300 to 7000 Td near the high-voltage electrode. The given values of the reduced field lie in a range that is optimal for ignition by discharge [16].

The high-voltage electric pulse was produced by a high-voltage pulse generator. The generator was assembled after the Marks scheme. The Marks generator consists of 15 stages with capacity of 6 nF. The amplitude of the output pulse was adjusted by a voltage of a charge power supply. The Marks generator was driven by an auxiliary spark generator. The amplitude and duration of the output pulse were measured by a back-current shunt and capacitive gauge (Fig. 28), which were mounted on a high-voltage feed line. The high-voltage line has coaxial geometry with water filling. The electric impedance of line Z was equal to 16 Ohm. The pulse reflected from the high-voltage electrode was not observed.

Five IR detectors are placed along the axis of the detonation tube. The detectors have a sensitivity range of 0.9–3.5 μm. They record IR emission of H_2O and CO_2. The flame speed was calculated from profiles of a voltage on the IR detectors, see Fig. 29. The speed of the detonation wave was measured with an accuracy of 80 m/s (3 %), and the speed of the deflagration wave was measured with an accuracy of 20 m/s (7 %).

The parameters of the initial gas (i.e., composition, pressure, and temperature) were measured in the experiments. The experiments were performed at initial pressures of 0.15–0.6 atm and ambient temperature in fuel mixtures: $C_3H_8 + 5O_2$ and $C_3H_8/C_4H_{10} + 5O_2 + xN_2$ ($0 \le x \le 10$), where C_3H_8/C_4H_{10} designates liquified petroleum gas (LPG).

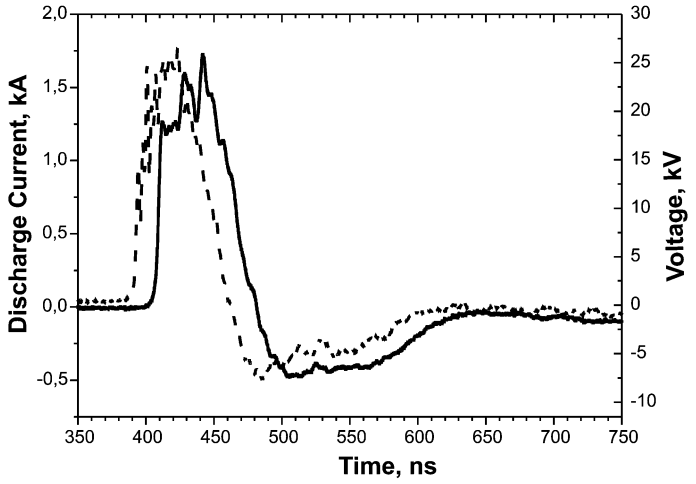

Fig. 28 Discharge current (solid line) and voltage (dashed line) dynamics.

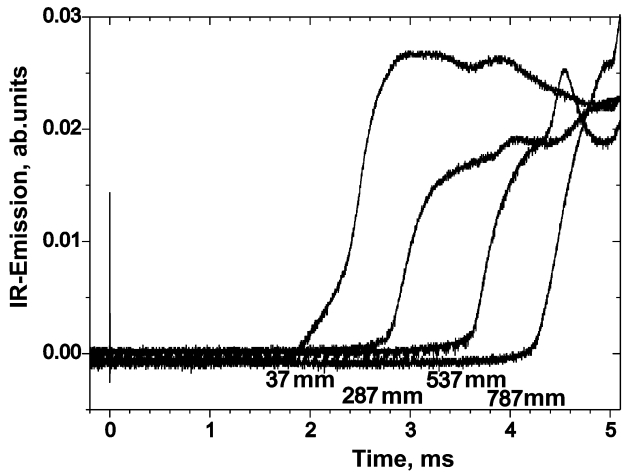

Fig. 29 Response of IR detectors. Mixture: $C_3H_8/C_4H_{10} + 5O_2$; pressure: 0.16 atm; speed: 300 m/s. Deflagration.

Ignition by nanosecond discharge

First, we studied the influence of nitrogen dilution on the ignition under the action of a nanosecond discharge [26]. We measured the induction time (Fig. 30) and the minimal ignition energy in mixtures $C_3H_8/C_4H_{10} + 5O_2 + xN_2$. The dependence is close to

$$\tau = \frac{1.1 \cdot 10^6}{\left(100\,\% - \left[N_2\right]\right)^3} \tag{7}$$

The nitrogen dilution has many effects, namely it: (1) decreases the ratio of the combustion heat to the heat capacity; (2) decreases the concentrations of fuel and oxygen; (3) increases the rate of recombination reactions; and (4) decreases the formation of active particles. At high temperatures (1200–1800 K), the delay time of autoignition depends on the nitrogen dilution at fixed pressure as $\sim(1 - [N_2])^{-x}$, where $x = 0.45$–0.65 [27]. In the case of autoignition, the second effect is the most promi-

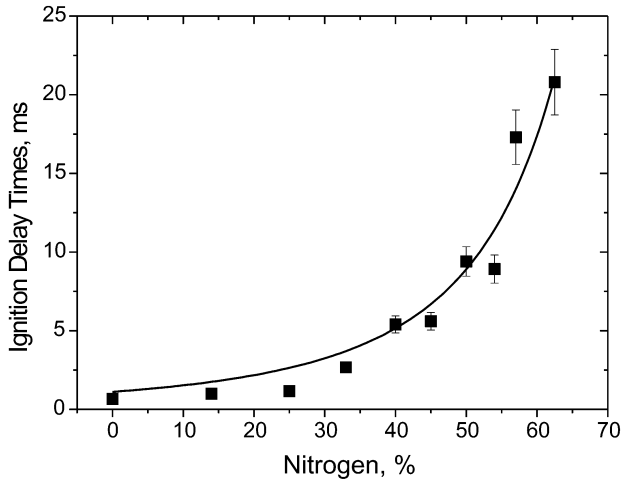

Fig. 30 Ignition delay time in mixtures $C_3H_8/C_4H_{10} + 5O_2 + xN_2$ at initial pressure 0.3 atm. Line corresponds to eq. 7.

nent. In our case, the nitrogen dilution not only acts on the chemical processes, but it reduces the generation of active species in the discharge. Probably, for the conditions of gas discharge initiation, the fourth factor is stronger than the other three.

The induction time and the minimal ignition energy have the same dependence on the percentage of nitrogen in the mixture at a fixed initial pressure (Fig. 31). The minimal ignition energy increases from 70 mJ for the nitrogen fraction of 25 % to 12 J for the nitrogen fraction of 62.5 %. The energy values of 0.07 and 12 J correspond to the minimal and maximal operating energies of our discharge device. The energy deposition of 0.07 J corresponds to heating of fuel mixture by 1 K. Thus, the mechanism of ignition is definitely nonthermal. There is a critical concentration of active species produced by discharge. The ignition initiated after concentration of active particles exceeds the critical value.

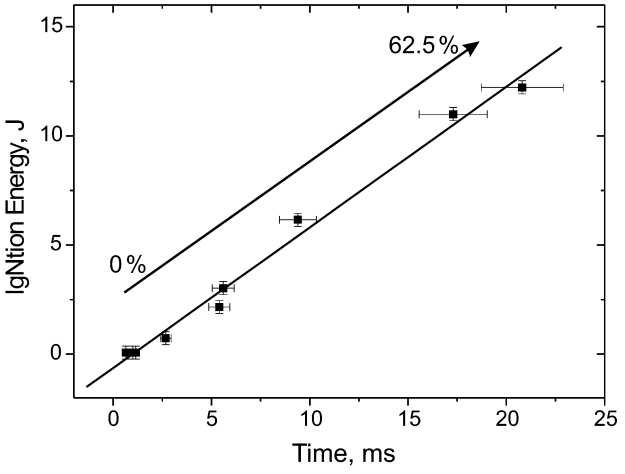

Fig. 31 Minimum ignition energy and ignition delay time for different nitrogen dilutions.

The minimal ignition energy extrapolated to nitrogen dilution of 77 % amounts to 25 J. The minimal ignition energy under excitation by a laser spark was measured in the work [28]. In a mixture of propane and air, the minimal ignition energy amounts to 4 mJ at a pressure of 0.3 atm. In our case, the high value of the minimal ignition energy is explained by a high volume of simultaneously ignited gas. The high-voltage nanosecond discharge is characterized by a low energy deposition per excited volume of gas in contrast to other types of discharge. In the experiments, this value was approximately equal to 0.3 J/l. The laser spark is more effective because it produces a very local spot. One hot spot is enough for ignition, but it is necessary to produce many hot spots to initiate detonation. The volume discharge is ineffective to initiate ignition at room temperature, but it is very promising for initiating detonation.

Figure 32 is a summary plot of the experiments in mixtures $C_3H_8/C_4H_{10} + 5O_2 + xN_2$ ($0 \le x \le 10$). Figure 32 depicts the speed of the flame front measured at 412 mm away from the discharge chamber. At relatively low pressures, we observed the deflagration wave with weak acceleration (Fig. 29). At relatively high pressures, we observed C-J detonation. At intermediate conditions, we observed transient detonation (Fig. 33). In this mode, the flame front strongly accelerates during its propagation along the tube. At conditions relative to Fig. 33, the speed of the flame front increases from 500 m/s at a position of 150 mm to 2000 m/s at position of 650 mm. The mode of flame front propagation is controlled by the initial pressure and mixture composition and is almost independent of the discharge energy (Fig. 34).

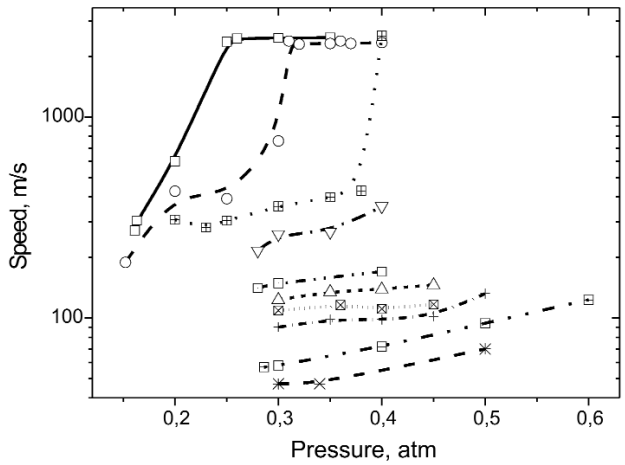

Fig. 32 Speed of the flame front at 412 mm away from discharge chamber in mixtures $C_3H_8/C_4H_{10} + 5O_2 + xN_2$. □: $x = 0$ (0 %); ○: $x = 1$ (14 %); ⊞: $x = 2$ (25 %); ▽: $x = 3$ (33 %); ⊡: $x = 4$ (40 %); △: $x = 5$ (45 %); ⊠: $x = 6$ (50 %); +: $x = 7$ (54 %); ⊟: $x = 8$ (57 %); *: $x = 10$ (63 %).

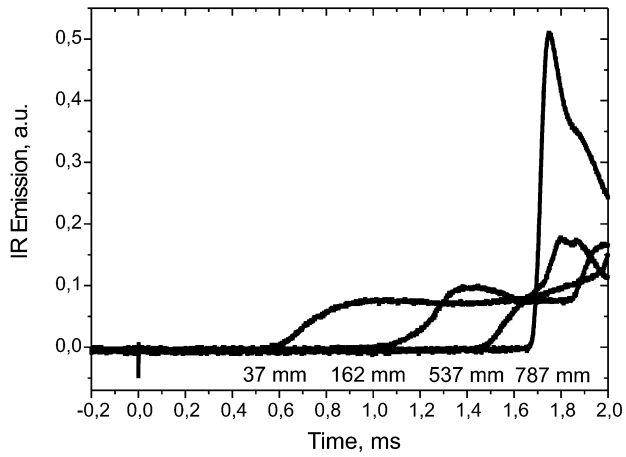

Fig. 33 Typical oscillograms from IR detectors. Mixture: C_3H_8/C_4H_{10} + $5O_2$ + N_2; pressure: 0.3 atm; speed: 400–1900 m/s. Transient detonation.

Formation of flame front

We have carried out observations of discharge development and formation of a flame front through the end plate of the detonation tube. The observations have been performed using ICCD camera LaVision PicoStar HR12. The camera registers emission within the wavelength range 300–800 nm. The $C^3\Pi_u$, $v' = 0 \rightarrow B^3\Pi_g$, $v'' = 0$ band of nitrogen mainly contributes to the intensity of the discharge emission at 337 nm.

The discharge development has three time stages. During the first stage, the emission intensity rises sharply. In the second stage, the emission intensity decreases. The third stage is the afterglow stage. The 1st, 2nd, and 3rd stages last ~10, ~50, and ~500 ns, respectively. The duration of the stages increases when the initial pressure rises. The initial stage of the discharge (up to 10 ns) is spatially quasi-homogeneous, while in the subsequent stages the discharge is localized over a few sections of the high-voltage electrode. In a 0.5–10 ms (in dependence to the initial conditions) after the discharge initiation, the mixture was ignited in the discharge chamber. In some sections, the ignition is stronger than in the others. Nevertheless, near the discharge chamber end plate, the mixture inflames simultaneously and the flame front covers the whole cross-section of the tube. The flame front position is determined by simultaneous measurements through the side-wall by IR sensors. When the flame front passes the distance equals to the diameter of the detonation tube from the discharge chamber, the front becomes spatially homogeneous over the cross-section of the tube.

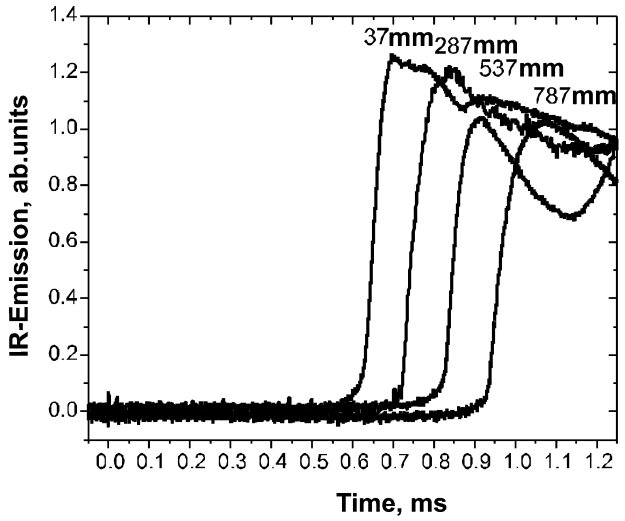

Fig. 34 Typical oscillograms from IR detectors. Mixture: $C_3H_8/C_4H_{10} + 5O_2$; pressure: 0.3 atm; speed: 2400 m/s. C-J detonation.

Initiation of detonation

Special experiments have been carried out to determine the conditions of detonation initiation. The experiments were performed in $C_3H_8 + 5O_2$ mixture at the initial pressure of 0.3 atm (Fig. 35). The length and time of DDT are equal. $L_{DDT} = 130$ mm and $t_{DDT} = 0.6$ ms at the initiation energy of the discharge of 70 mJ. The initiation energy per cross-section is equal to 4 J/m^2.

In our case, the initiation of detonation proceeds during two stages. During the first stage, the nanosecond discharge excites the gas in the discharge chamber. In the second stage, a chemical energy of about 1 kJ releases after an ignition delay of 0.5–20 ms. The released energy is enough to initiate detonation under appropriate conditions. The discharge produces active species near high-voltage electrodes. The gradient of active species concentration [23] and near-simultaneous energy release [17] assist initiating detonation.

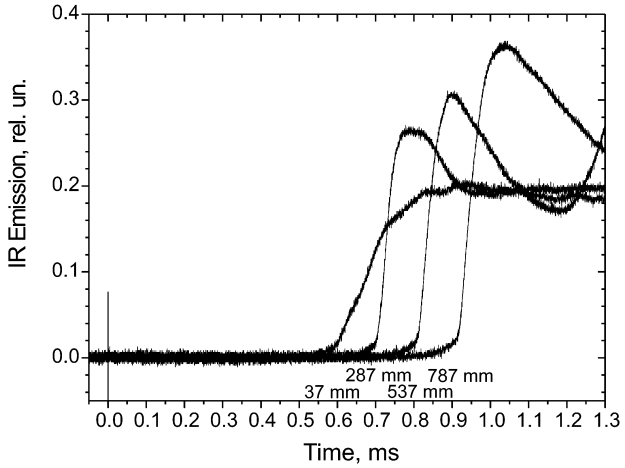

Fig. 35 Typical oscillograms from IR detectors. Mixture: $C_3H_8 + 5O_2$; pressure: 0.3 atm; speed: 2380 m/s. C-J detonation.

CONCLUSIONS

The kinetics of slow oxidation of alkanes under the action of the nanosecond pulsed-periodic discharge in stoichiometric and lean mixtures with oxygen and air at room temperature has been investigated experimentally.

It has been shown that for the total pressure of mixture lower than the pressure of maximal energy input (which is 3 Torr in our case), the discharge has developed at the background of the high cathode drop that has caused essential nonuniformity of energy contribution. For pressures starting with the pressure of maximal energy input, the main part of energy is contributed at the stage of the short circuit of the discharge where the cathode drop is negligible and the electric field and the current do not vary along the DC, and thus these features guarantee uniformity of energy contribution.

It has been shown that the alkanes under nanosecond discharge at ambient temperature are entirely oxidized. The times of complete oxidation with the same values of energy contribution, mixture initial pressure, and equivalence ratio did not differ for any alkanes larger than methane. Methane oxidation was twice slower than the other alkanes. Alkane oxidation in mixtures with oxygen occurs approximately twice more effectively than in corresponding mixtures with air. The times of full oxidation of alkanes are proportional to the equivalence ratio under our conditions.

The study of the efficiency of nanosecond discharge plasma on combustion and ignition process has been carried out. The following conclusions can be made.

A double propane–air flame blow-off velocity increase has been obtained for nanosecond plasma-assisted combustion, with the energy input negligible in comparison with the burner's chemical power (less than 0.5 %). It has been experimentally shown that the results for methane–air flame are similar to the propane–air one. Moreover, a proper form of energy input and a proper organization of discharge are of great importance. It has been found that the effectiveness of plasma-assisted combustion depends on the type of discharge, pulse duration, pulse repetition rate, and other parameters that are responsible for active particle production. It has been determined that active particles (O and OH primarily), which are produced in the streamer head under its action, play the most significant role in combustion acceleration.

The investigation of the efficiency of the nanosecond discharge to ignite a homological family of hydrocarbons has been started. Gas mixtures of methane, propane, and butane have been investigated under the same experimental conditions. It has been demonstrated that a high-voltage nanosecond discharge is an efficient tool of ignition of different hydrocarbons. The results for the ignition delay and shift of the temperature threshold under nanosecond discharge have been obtained experimentally.

The experimental demonstration of application of high-voltage nanosecond gas discharge to initiate detonation has been performed. A pulsed nanosecond discharge initiates detonation within the DDT length down to 130 mm in a tube with a diameter of 140 mm. Detonation is initiated by energy of 70 mJ (4 J/m^2) in mixture $C_3H_8 + 5O_2$ under initial pressure of 0.3 atm.

The measurements of the minimal ignition energy and ignition delay time have been performed in $C_3H_8/C_4H_{10} + 5O_2 + xN_2$ ($0 \le x \le 10$) mixtures within the pressure range 0.15–0.6 atm. The minimal ignition energy and ignition delay time strongly depend on nitrogen dilution to initiate ignition by a high-voltage nanosecond discharge. The extrapolated value of minimal ignition energy amounts to 25 J at the dilution level of 77 %.

The spatially homogeneous discharge is not a very effective tool to initiate slow flame, and applying such discharges can be greatly advantageous to initiate high-speed flames and detonation. The mode of the flame front propagation is controlled by initial pressure, mixture composition, and discharge distribution, but it is independent of the discharge energy.

The discharge has different intensity in the sections of the discharge chamber. After ignition, the flame front occupies the whole cross-section of the detonation tube almost simultaneously, and the nonuniformity of the flame front diminishes completely during the formation of the detonation wave front.

ACKNOWLEDGMENTS

This work was partially supported by grants of RFBR/NWO 03SRF08, RFBR 05-03-32975, 05-02-17323, EOARD/CRDF PR0-1349-MO-02, and CRDF MO-011-0.

The authors are grateful to Vladimir Khorunzhenko, Nikolay Mazko, and Vyacheslav Zudov for their assistance in adjustment of the equipment and fruitful discussions.

REFERENCES

1. N. N. Semenov. Nobel Lecture, 11 Dec. 1956: <http://www.nobel.se/chemistry/laureates/>.
2. L. S. Polak, A. A. Ovsiannikov, D. I. Slovetskii, F. B. M. Vurzel. *Theoretical and Applied Plasmochemistry*, p. 222, Nauka, Moscow (1975).
3. D. A. Eichenberger, W. L. Roberts. *Combust. Flame* **118**, 469 (1999).
4. E. C. Samano, W. E. Carr, M. Seidl, B. S. Lee. *Rev. Sci. Instrum.* **64**, 2746 (1993).
5. N. B. Anikin, S. M. Starikovskaia, A. Yu. Starikovskii. *J. Phys. D.: Appl. Phys.* **34**, 177 (2001).
6. N. B. Anikin, S. M. Starikovskaia, A. Yu. Starikovskii. "Oxidation of C_1-C_{10} hydrocarbons in stoichiometric and lean mixtures with air and oxygen under the action of nanosecond discharge", 43rd AIAA Aerospace Sciences Meeting and Exhibit, Reno, NV, USA (2005).
7. Yu. P. Raizer. *Physics of Gas Discharge*, Nauka, Moscow (1992).
8. S. V. Pancheshnyi, S. M. Starikovskaia, A. Yu. Starikovskii. *J. Phys. D.: Appl. Phys.* **32**, 2219 (1999).
9. E. I. Mintoussov, S. V. Pancheshnyi, A. Yu. Starikovskii. "Propane-air flame control by non-equilibrium low-temperature pulsed nanosecond barrier discharge", 42nd AIAA Aerospace Sciences Meeting and Exhibit, Reno, NV, USA (2004).
10. M. M. Nudnova, S. V. Pancheshnyi, A. Yu. Starikovskii. "Pressure dependence of the development of cathode-directed streamer", XV International Conference on Gas Discharges and their Applications, Toulouse, France (2004).
11. S. Pellerin, J. M. Cormier, F. Richard, K. Musiol, J. Chapelle. *J. Phys. D.: Appl. Phys.* **29**, 726 (1996).
12. K. P. Huber, G. Herzberg. *Molecular Spectra and Molecular Structure. IV. Constants of Diatomic Molecules*, Litton Educational Publishing (1979).
13. S. M. Starikovskaia, I. N. Kosarev, A. V. Krasnochub, E. I. Mintoussov, A. Yu. Starikovskii. "Control of combustion and ignition of hydrocarbon-containing mixtures by nanosecond pulsed discharges", 43rd AIAA Aerospace Sciences Meeting and Exhibit, Reno, NV, USA (2005).
14. G. L. Schott, J. L. Kinsey. *J. Chem. Phys*. **29**, 1177 (1958).
15. K. A. Bhaskaran, P. Roth. *Prog. Energy Combust. Sci.* **28**, 151 (2002).
16. S. A. Bozhenkov, S. M. Starikovskaia, A. Yu. Starikovskii. *Combust. Flame* **133**, 133 (2003).
17. E. Schultz, E. Wintenberger, J. E. Shepherd. In *Proc. of the 16th JANNAF Propulsion Symposium*, Chemical Propulsion Information Agency (1999).
18. C. J. Brown, G. O. Thomas. *Shock Waves* **10**, 23 (2000).
19. R. Sorin, R. Zitoun, D. Desbordes. "Optimisation of the deflagration to detonation transition: Reduction of length and time of transition", Paper 142 at 19th ICDERS, Hakone, Japan, 17 July–1 August 2003.
20. S. I. Jackson, J. E. Shepherd. 38th AIAA/ASME/SAE/ASEE Joint Propulsion Conference and Exhibit, 7–10 July 2002, Indianapolis, USA.
21. J. E. Shepherd, J. M. Austin, T. Chao, F. Pintgen, E. Wintenberger, S. Jackson, M. Cooper. "Detonation initiation and propagation", 15th ONR Propulsion Conference, Washington DC, August 2002.
22. N. N. Smirnov, V. F. Nikitin. *Combust., Explosion, Shock Waves* **40**, 186 (2004).

23. Ya. B. Zeldovich, V. B. Librivich, G. M. Makviladze, G. I. Sivashinskii. *J. Appl. Mech. Tech. Phys*. **11**, 76 (1970).
24. J. B. Liu, P. D. Ronney, M. A. Gundersen. "Premixed flame ignition by transient plasma discharges", 29th International Symposium on Combustion, Sapporo, Japan, 21–26 July 2002.
25. F. Wang, C. Jiang, A. Kuthi et al. "Transient plasma ignition of hydrocarbon-air mixtures in pulse detonation engines", 42nd AIAA Aerospace Sciences Meeting and Exhibit, Reno, NV, 5–8 Jan. 2004.
26. V. P. Zhukov, A. Yu. Starikovskii. "Deflagration-to-detonation control by non-equilibrium gas discharges and its applications for pulsed detonation engine", 43rd AIAA Aerospace Sciences Meeting and Exhibit, Reno, NV, USA (2005).
27. N. Lamoureux, C. E. Paillard, V. Vaslier. *Shock Waves* **11**, 309 (2002).
28. T. W. Lee, V. Jain, S. Kozola. *Combust. Flame* **125**, 1320 (2001).